Journal of Alloys and Compounds 969 (2023) 172431

Contents lists available at ScienceDirect

Journal of Alloys and Compounds

journal homepage: www.elsevier.com/locate/jalcom

α-MnO_2 composite with gold nanoparticles on carbon cloth modified with MOFs-derived porous carbon for flexible and activity-enhanced sodium-ion supercapacitors

Hanxue Zhao [a,1], Kaishuai Yang [c,1], Kailan Zhu [a,1], Mai Li [a,*], Wendong Xu [a], Waqar ul Hasan [a], Jiale Wang [a], Qinglin Deng [b,*], Jun Yu [d], Zhongyi Sun [d], Paul K. Chu [e]

[a] College of Science, Donghua University, Shanghai 201620, China
[b] School of Physics and Materials Science, Guangzhou University, Guangzhou 510006, China
[c] School of Electronic and Information Engineering, Changshu Institute of Technology, Suzhou 215000, China
[d] Semiconductor New Materials Research and Development Center, SHANGHAI Q-TECH CO., LTD., Zhengxue Road, Yangpu District, Shanghai, China
[e] Department of Physics, Department of Materials Science and Engineering, and Department of Biomedical Engineering, City University of Hong Kong, Tat Chee Avenue, Kowloon, Hong Kong, China

ARTICLE INFO

Keywords:
Flexible electrode
Manganese dioxide
Carbon nanoflakes
Gold particles
Sodium-ion supercapacitor

ABSTRACT

Improving the catalytic activity of electrodes in a limited space is crucial to energy storage devices such as supercapacitors. Herein, the surface activity of the flexible electrode (Au-MnO_2/CPCN@CC) is enhanced by combining gold particles (AuNPs) modified α-MnO_2 with conductive porous carbon nanoflakes (CPCN) derived from the metal-organic framework (MOF) on carbon cloth (CC). The Au-MnO_2/CPCN@CC electrode exhibits a higher specific capacity of 503.7 F/g at 0.125 mA/cm^2 and retains 87.68% capacity after 10,000 cycles in 1 M Na_2SO_4, while the structure without AuNPs achieves 242.6 F/g and 61.07% capacity retention after 10,000 cycles. The high stability of Au-MnO_2/CPCN@CC stems from the good pseudocapacitance ratio of 83.80% at 1 mV/s compared to 78.43% of MnO_2/CPCN@CC and 40.88% of Au/CPCN@CC. The supercapacitor assembled with Au-MnO_2/CPCN@CC as the positive electrode and activated carbon (AC) as the negative electrode in 1 M $NaPF_6$ shows an excellent power density of 79.96 W/kg at 71.48 Wh/kg as well as 81.93% capacitance retention after 10,000 cycles. Density-functional theory (DFT) calculations of Au-MnO_2/CPCN composite reveal a sodium-ion adsorption energy of 3.744 eV and a large DOS near Fermi level. Hence, Au nanoparticles (AuNPs) and MOFs-derived CPCN lead to enhanced surface electron transport of MnO_2 and ultimately superior performance.

1. Introduction

Although the surface activity of electrodes in energy storage devices continues to improve [1–6], the development of high-performance electrodes with fast electron transfer kinetics for supercapacitors that meet the requirements of fast charging/discharging, high power density is still challenging [7,8]. The electrode materials, structure, and electrolytes determine the overall properties of supercapacitors. Carbonaceous materials [9,10], metal oxides [11,12], and conducting polymers [13,14] are promising electrode materials for supercapacitors. Among them, carbonaceous materials such as carbon aerogel [15], graphene [16], carbon nanofibers [17], and activated carbon [18] are common in supercapacitors because of the abundant resource, variable pore size, large specific surface area, good thermal stability, and good electrical conductivity. Owing to the complex properties of carbonaceous materials, issues related to nano-crystallization, porosity, surface modification, and composition of the active materials must be addressed in the preparation of carbon-based electrodes for flexible supercapacitors [19].

Conductive porous carbon nanoflakes (CPCN) derived from the metal-organic framework (MOF) have been used to form the electrode skeleton because of their excellent structural regulation ability [20–22]. By using organic ligands and metal ions as the precursors, MOFs are fabricated as crystalline materials with self-assembled and adjustable structures boasting a large specific surface area and good conductivity [23–25]. By modulating the functional groups and the ratio of metal ions/metal clusters and organic ligands, the morphology and

* Corresponding authors.
E-mail addresses: limai@dhu.edu.cn (M. Li), qldeng@gzhu.edu.cn (Q. Deng).
[1] These authors contributed equally to this work

https://doi.org/10.1016/j.jallcom.2023.172431
Received 15 July 2023; Received in revised form 3 October 2023; Accepted 4 October 2023
Available online 6 October 2023

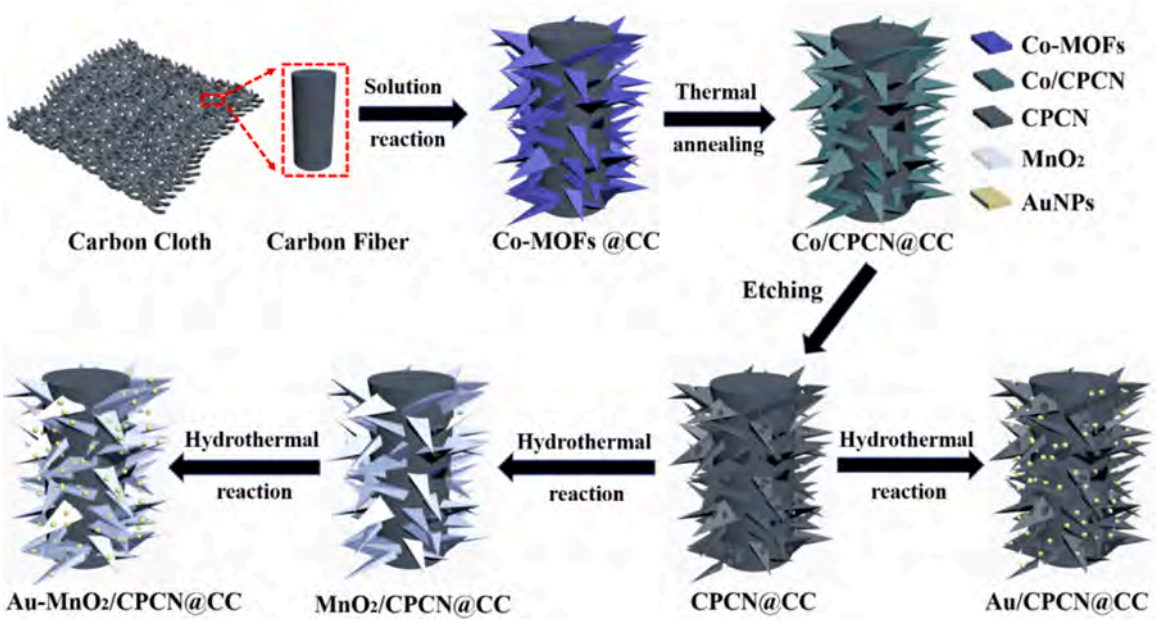

Fig. 1. Schematic illustration of electrode fabrication.

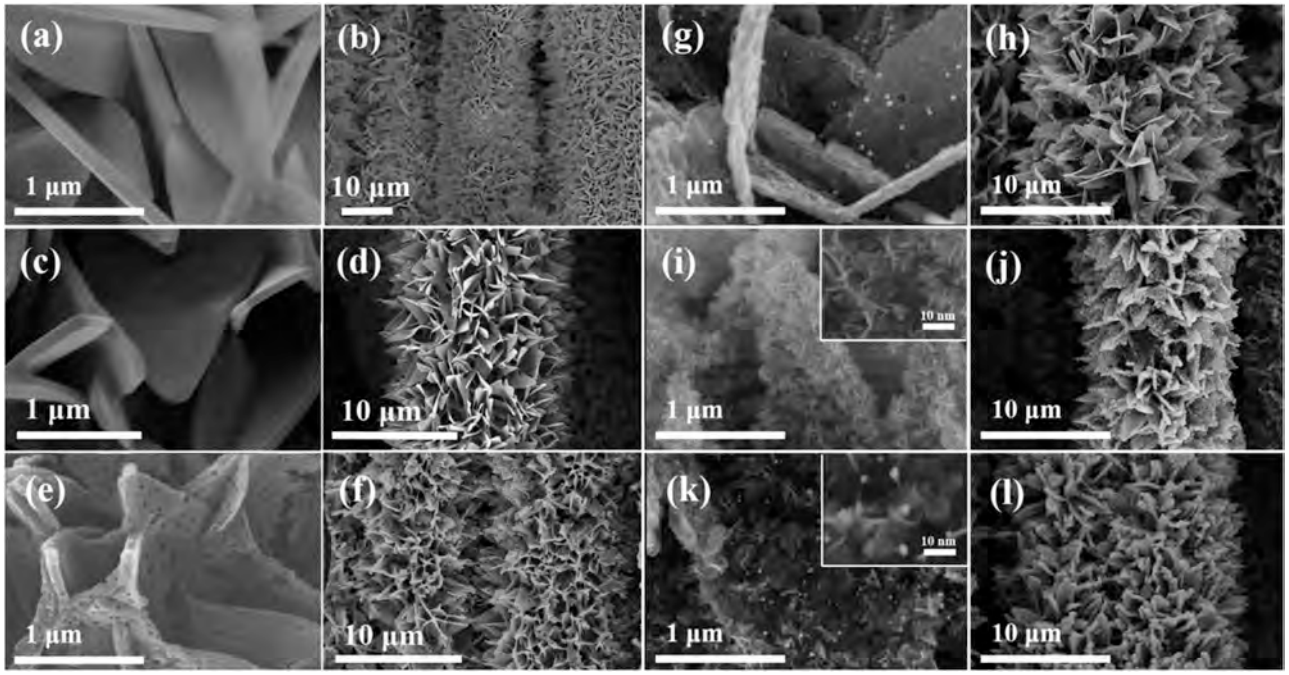

Fig. 2. SEM images of (a-b) Co-MOFs@CC, (c-d) Co/CPCN@CC, (e-f) CPCN@CC, (g-h) Au/CPCN@CC, (i-j) MnO_2/CPCN@CC, and (k-l) Au-MnO_2/CPCN@CC.

composition of MOFs can be modulated. By optimizing the preparation process, MOF nanosheets with a large surface area can be deposited evenly on the carbon cloth (CC). High-temperature carbonization and metal ion etching produce the 3D carbon skeleton of CPCN with a large surface area and porous structure that improves the electrolyte mobility and loading capacity of the active materials. Wang et al. [26] have synthesized Ni-MOF with hierarchical flower-like structure by solvent-assisted approach that prepares high specific capacitance and excellent rate performance. Salunkhe et al. have prepared nanoporous carbon from cobalt-based MOFs (ZIF-67) by controlling the annealing conditions and composed them with Co_3O_4 to form asymmetric supercapacitors with a high specific energy (36 Wh/kg,1600 W/kg) [21]. Nevertheless, the properties of CPCN still cannot meet the requirements of supercapacitors and a more effective means to improve the efficiency by integrating CPCN with pseudo-capacitor materials is important.

As a type of surface-redox pseudocapacitive materials, MnO_2 has merits such as the high theoretical capacitance, tunable surface structure, and low cost [13,27–29]. However, in practical applications, the low electron conductivity makes the actual capacity of MnO_2 lower than expected [30–32]. Moreover, MnO_2 is prone to structural degradation during charging/discharging as a result of dissolution and agglomeration of manganese dioxide [31]. Currently, the cyclic stability and specific capacitance of MnO_2 are typically optimized by combining with high-conductivity materials [33,34], formation of special surface morphology [35,36], metal doping, and surface modification [37]. Yang et al. [38] have fabricated MnO_2 nanosheets on nickel foam by

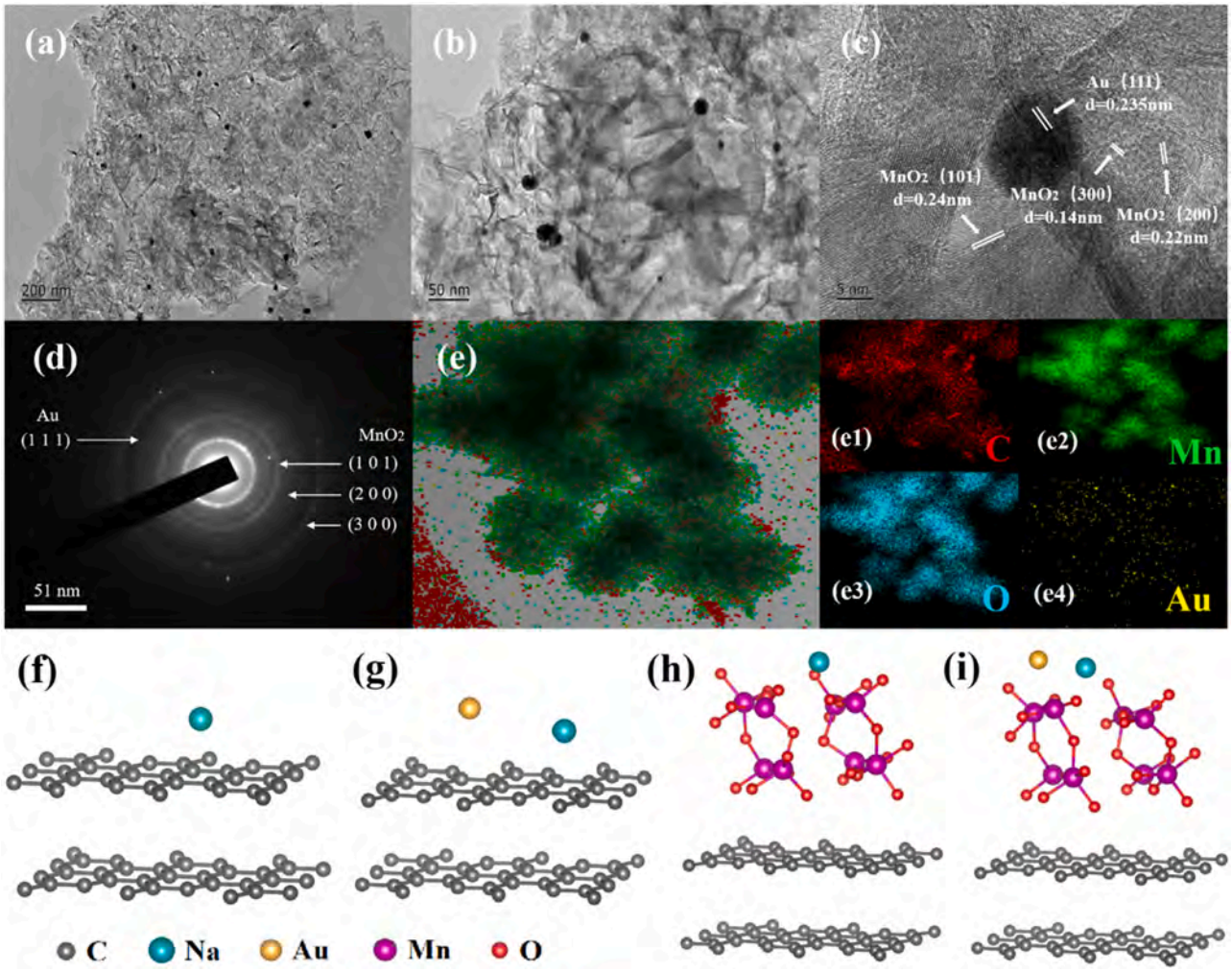

Fig. 3. (a, b) TEM images of the Au-MnO_2/CPCN nanocomposite at different magnifications; (c) HR-TEM image and (d) SAED image of the Au-MnO_2/CPCN nanocomposite; (e) EDS elemental map of the Au-MnO_2/CPCN nanocomposite; (e1) EDS C map, (e2) EDS Mn map, (e3) EDS O map, and (e4) EDS Au map; the Atomic structures of (f) CPCN, (g) Au-CPCN, (h) MnO_2/CPCN and (i) Au-MnO_2/CPCN;.

electrodeposition, which forms a porous three-dimensional network with an orderly arrangement between layers. The area-specific capacitance of MnO_2 at 2 mA/cm^2 is 279 F/cm^2. Therefore, constructing MnO_2 with a carbon skeleton like CPCN is an effective way to improve the conductivity and loading of MnO_2. Meanwhile, in order to enhance electron transport between the active surface and electrolyte, gold nanoparticles (AuNPs) can be deposited on MnO_2. The specific capacitance of Au-MnO_2/CNT synthesized by Reddy et al. [39] is 106 F/cm^2, which is improved compared to that of MnO_2/CNT of 69 F/cm^2, and the equivalent resistances MnO_2/CNT and Au-MnO_2/CNT are 7.3 Ω/cm^2 and 2.5 Ω/cm^2, respectively.

Gold nanoparticles (AuNPs) which are spheroidal particles with a diameter of about 20 nm offer advantages such as high electronic conductivity, easy synthesis, and high stability [40,41]. Khandare et al. [42] have prepared crystalline MnO_2 fibers 10 μm long and 20 nm wide by chemical methods. They have also produced AuNPs-modified MnO_2 materials by simple deposition for electrodes in supercapacitors which show a specific capacitance of 267 F/g that is more than five times higher than the 50 F/g specific capacitance of pure MnO_2 for a Au size of approximately 29 nm. However, there have been few reports on the direct application of AuNPs on MOFs-derived carbon based MnO_2 to supercapacitors because the main obstacle is the poor binding force between MnO_2 and carbon, so that MnO_2 will fall off during deposition of AuNPs at a high temperature under magnetic stirring. Therefore, common MOFs-derived carbon techniques are obviously not suitable.

In this study, a novel structure composed of α-phase ultrathin MnO_2 films prepared on a piece of carbon fiber cloth modified with MOFs derived CPCN (CPCN@CC) is designed and fabricated as the MnO_2/CPCN@CC electrode, and AuNPs are deposited on MnO_2/CPCN@CC to form Au-MnO_2/CPCN@CC, as shown in Fig. 1 [43,44]. The combination of CPCN and AuNPs offers advantages such as a large surface area, efficient ion diffusion, large active substance loading, and excellent conductivity. The electrochemical properties are assessed and confirmed by density-functional theory (DFT) calculations. To confirm the practical feasibility, an asymmetric supercapacitor (ASC) is assembled with Au-MnO_2/CPCN@CC as the negative electrode, carbon cloth coated with activated carbon (AC@CC) as the positive electrode, and 1 M $NaPF_6$ electrolyte commonly used in commercial sodium-ion supercapacitors for the 4 V window. The electrochemical properties and mechanisms are investigated and discussed.

2. Experimental details

2.1. Material synthesis

The fabrication procedure and schematic structure of Au-MnO_2/CPCN@CC are depicted in Fig. 1. The cobalt-based MOFs were prepared on CC by mixing 50 mM $Co(NO_3)_2{\cdot}6\,H_2O$ of and 400 mM 2-methylimidazole (2-MIM) in equal volumes to form the precursor solution and then the carbon cloth was soaked in the solution for 4 h at room

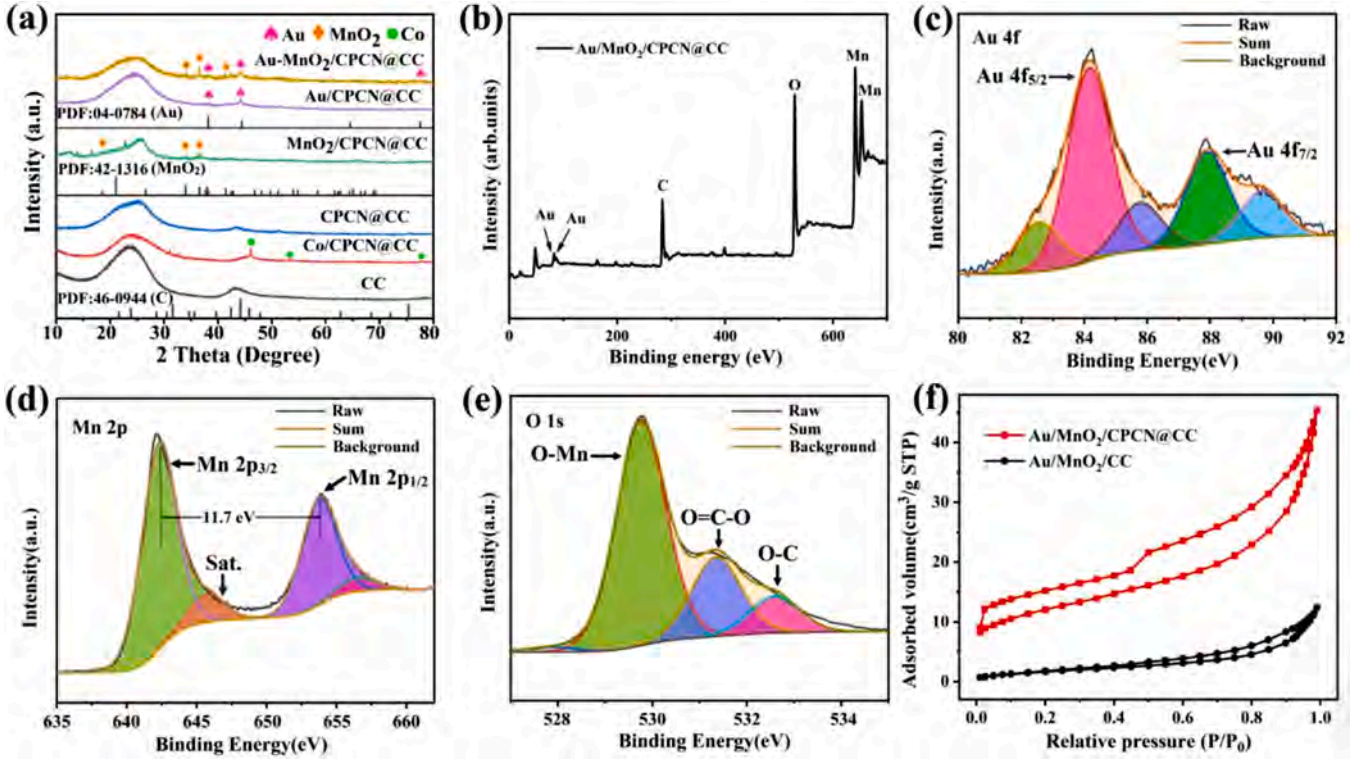

Fig. 4. (a) XRD spectra of CC, Co/CPCN@CC, CPCN@CC, Au/CPCN@CC, MnO_2/CPCN@CC, and Au-MnO_2/CPCN@CC; Au-MnO_2/CPCN@CC; (b) Survey XPS spectrum; High-resolution XPS spectra of (c) Au 4 f, (d) Mn 2 p, and (e) O 1 s; (f) N_2 adsorption-desorption isotherm of Au-MnO_2/CC and Au-MnO_2/CPCN@CC.

temperature. The carbon cloth was rinsed successively with alcohol and deionized (DI) water and dried at 60 °C for 12 h to obtain Co-MOFs@CC, which was then annealed at 950 °C for 2 h under N_2 to form Co/CPCN@CC. Co/CPCN@CC was placed in an autoclave containing 6 M HNO_3 for 24 h at 100 °C to etch Co^{2+} and retain the carbon skeleton derived from the MOFs. After etching, the sample was rinsed three times with alcohol and DI water and dried at 60 °C for 12 h to obtain CPCN@CC. CPCN@CC was placed in a PTFE vessel containing DI water, 5.0 mM $KMnO_4$, and 1.9 mM $MnSO_4$, sealed, placed in a reactor, and heated to 140 °C for 3 h. After cooling to room temperature naturally, the product was rinsed several times with DI water and dried at 70 °C for 12 h to produce the electrode of MnO_2/CPCN@CC. In order to deposit the AuNPs on the electrode, 48 ml of DI water, 1 ml of 34.0 Mm $C_6H_5Na_3O_7{\cdot}2\,H_2O$, and 1 ml of 1.3 Mm polyvinylpyrrolidone (PVP) were added to the flack and stirred. After the DI water boiled in the flack, 62.5 μL of 200 mM $HAuCl_4{\cdot}3\,H_2O$ and MnO_2/CPCN@CC or CPCN@CC were added successively and boiled for 30 min under magnetic stirring. After the reaction, the samples were taken out and dried at 60 °C for 3 h to obtain the electrodes of Au-MnO_2/CPCN@CC or Au/CPCN@CC.

2.2. Materials characterization

The morphology, structure, and elemental composition of the electrodes were examined and determined by scanning electron microscopy (SEM) on the S4800 (HITACHI, Tokyo, Japan), energy dispersive X-ray spectrometry (EDS) on the JEM 2100 F (JEOL, Tokyo, Japan), selected-area electron diffraction (SAED) on the X-MAX 80TLE (Oxford Instruments, Oxford, England), transmission electron microscopy (TEM) on the JEM 2100 F (JEOL, Tokyo, Japan) at 200 kV, and energy dispersive X-ray spectroscopy (EDS) on the JEM 2100 F (JEOL, Tokyo, Japan). The crystal structure was determined by X-ray diffraction (XRD) on the D/max-2550VB+ /PC (Rigaku, Tokyo, Japan). To measure the chemical states and composition, X-ray photoelectron spectroscopy (XPS) was carried out on the ESCALB 250XI (Thermo Fisher, Waltham, MA USA). Nitrogen adsorption desorption isotherm data were obtained using a Autosorb-iQ at 77 K.

2.3. Electrochemical measurements

The electrochemical evaluation was carried out on the CHI660E electrochemical workstation. Using 1.0 M Na_2SO_4 as the electrolyte, CC, CPCN@CC, and MnO_2/CPCN@CC or Au-MnO_2/CPCN@CC were the working electrodes, while a saturated calomel electrode was the reference electrode and platinum wire was the counter electrode. The mass loading was 2.86 mg/cm^2. Cyclic voltammetry (CV), galvanostatic charging-discharging (GCD), and electrochemical impedance spectroscopy (EIS) were carried out to determine the electrochemical properties. The mass specific capacity(C_m, F/g) and area capacitance (C_a, F/cm^2) were assessed by constant current charging and discharging (GCD) according to Eqs. (1) and (2) [45]:

$$C_m = \frac{It}{m\Delta V} \tag{1}$$

$$C_a = \frac{It}{S\Delta V}, \tag{2}$$

where ΔV is the discharging voltage window, t is the discharging duration (s), I is the discharging current (A), m is the mass of the active materials (g), and S is the surface area (cm^2).

An asymmetric supercapacitor (ASC) based on the two-electrode system was assembled in an argon-filled glove box with an electrolyte of 1.0 M $NaPF_6$ with EC: PC = 1: 1 vol% and 5% FEC. The energy density (E, W·h/kg) and power density (P, W/kg) were calculated by Eqs. (3) and (4) [46,47]:

$$E = \frac{C_m V^2}{2} \times \frac{1000}{3600} \tag{3}$$

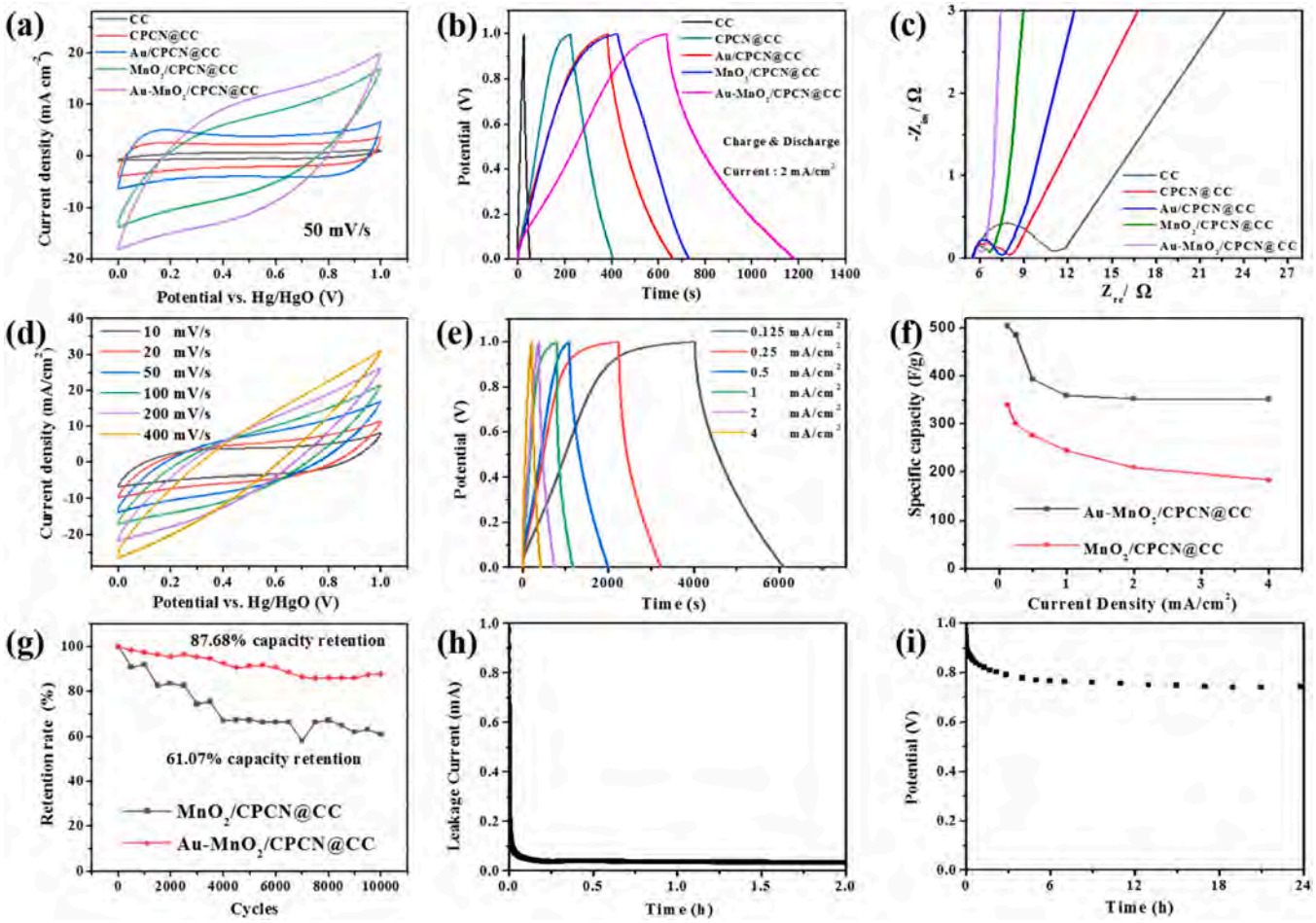

Fig. 5. Electrochemical results of the electrodes. (a) CV, (b) GCD and (c) EIS curves of CC, CPCN@CC, Au/CPCN@CC, MnO_2/CPCN@CC, and Au-MnO_2/CPCN@CC; (d) CV curves (e) GCD curves of Au-MnO_2/CPCN@CC; (f) Specific capacity at different current densities and (g) cycling stability of Au-MnO_2/CPCN@CC and MnO_2/CPCN@CC; (h) Leakage current and (i) Self-discharging curve of Au-MnO_2/CPCN@CC.

$$P = \frac{3600E}{\Delta t} \quad , \tag{4}$$

where Δt denotes the discharge time(s) and V is the voltage window(V).

2.4. Density-functional theory calculations

The calculations were performed by the density-functional theory (DFT) implemented in the Vienna ab initio simulation package (VASP) [48,49]. The project-augmented-wave (PAW) [50] and Perdew-Burke-Ernzerhof (PBE) generalized gradient approximation (GGA) [51] methods were implemented to treat the pseudopotentials and exchange correlation functionals. A plane wave cutoff of 520 eV was set for the kinetic energy and all self-consistent field computations were performed with a convergence criterion of 1×10^{-5} eV. In order to calculate the adsorption energies of sodium ions on CPCN, Au/CPCN, MnO_2/CPCN and Au-MnO_2/CPCN, four computational models of rectangular parallelepipeds with dimensions of 8.5 Å × 4.9 Å× 25 Å were constructed. The models consisted of carbon layer, carbon layer with a gold ion, carbon layer connected by a MnO_2 layer, and carbon layer connected by a MnO_2 layer with a gold ion, respectively. The thickness of the MnO_2 layer was 5.3 Å. To eliminate the interactions of the adjacent periodic images, each model was separated by a 15 Å vacuum layer in the z-axis and the Monkhorst-Pack [52] k-mesh of 4 × 7 × 1 was used in the Brillouin zone integration.

3. Results and discussion

The SEM images of the electrodes in different stages are depicted in Fig. 2 and Fig. S1. As shown in Fig. 2(a-b), MOFs nanosheet grow uniformly on CC substrate, and the thickness measured by Digital Micrograph is about 200 nm. The MOFs at high temperature is converted into a mixture of carbon nanoflakes and cobalt with a thickness around 100 nm uniformly covering the surface of CC (Fig. 2(c-d)), which providing an excellent template for the fabrication of conductive porous carbon nanoflakes. The decrease in the thickness of the MOFs sheets caused by the decomposition of the precursor during calcination results in a decrease in the resistance. In addition, calcination enhances the stability and adhesion of MOF precursors to CC. Fig. 2(e-f) present the images of annealed carbon nanosheets after nitric acid etching. It can be seen that there are pores on the carbon nanosheets to form three-dimensional porous carbon skeleton, which increasing the surface area of CPCN@CC.

The special carbon structure yields noteworthy enhancement in the overall electrochemical properties of the electrodes and supercapacitors by increasing the contact area between the active materials and electrolyte. To provide experimental proof, Fig. 2(g-h) depict the electrode composed of AuNPs grown directly on CPCN@CC for comparison. Fig. 2 (i-j) show the images of MnO_2/CPCN@CC, MnO_2 nanosheets are uniformly deposited on CPCN@CC, and the special three-skeleton structure of CPCN@CC increases the contact area between MnO_2 and electrolyte. Additionally, Fig. 2(k-l) and Fig. S1 exhibit the images of the Au-MnO_2/CPCN@CC electrode on which AuNPs with a diameter of 30 nm are

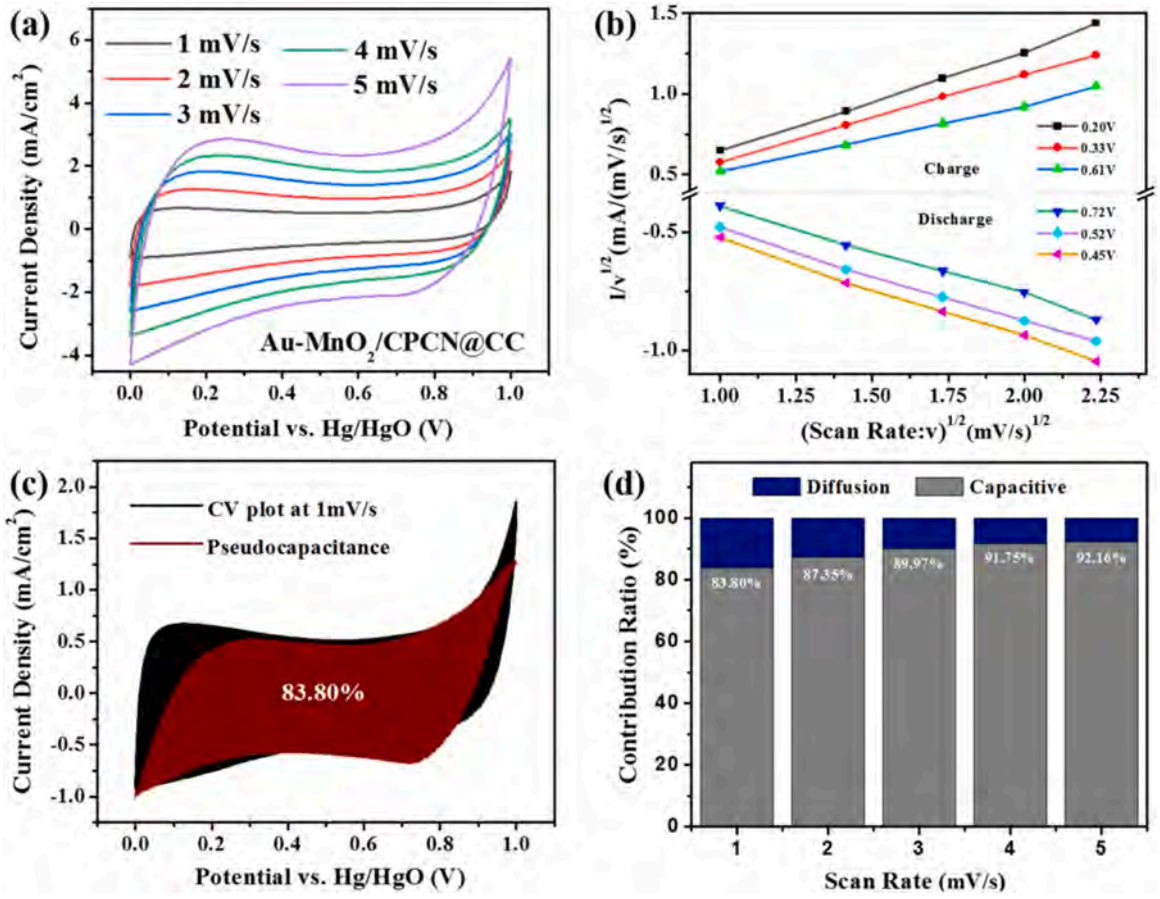

Fig. 6. Pseudocapacitance duty ratio analysis of Au-MnO_2/CPCN@CC. (a) CV curves; (b) Current versus voltage in the CV curves; (c) Pseudocapacitance duty ratios of the composite electrode at a scanning rate of 1 mV/s; (d) Pseudocapacitance duty ratio plot.

evenly distributed and Fig. S1(f) confirms large-area deposition. As a result of the porous structure and functional groups on CPCN, MnO_2 attaches firmly during the deposition of AuNPs at the high temperature under stirring. The synergistic effects of AuNPs and CPCN enable swift electron and ion transport and promote the redox reactions.

The Au-MnO_2/CPCN@CC core–shell structure is stripped ultrasonically to perform TEM, SAED, and EDS. Fig. 3(a-b) shown that Au-MnO_2/CPCN@CC is composed of gold particles and MnO_2 nanosheets, MnO_2 nanosheets were uniformly and densely deposited on CPCN and the AuNPs with a diameter of about 30 nm are in tight contact with MnO_2, which is consistent with those observed by SEM. The high-resolution image in Fig. 3(c) indicates lattice spacings of 0.14 nm, 0.22 nm, and 0.24 matching the (111), (200), and (101) planes of MnO_2, respectively, and 0.235 nm for the (111) plane of Au. Fig. 3(d) shows that manganese dioxide is not single-crystal and the radii of the three rings are 0.24, 0.22, and 0.14 nm corresponding to the (101), (200), and (300) planes of MnO_2, respectively, together with d = 0.235 nm for the Au (111) plane. Fig. 3(e) shows the presence of Mn, C, O, and Au and MnO_2 is coated uniformly onto CPCN and AuNPs are also uniformly distributed on MnO_2. These results indicate successful synthesis of the nitrogen-doped Au-MnO_2/CPCN structure. In order to bridge the gap between theory and practice, a series of electrode atomic models were established based on the material structure analysis results obtained through XRD and TEM. The subsequent theoretical analysis was conducted based on these models. Fig. (f)-(i) represent CPCN, Au-CPCN, MnO_2/CPCN, and Au-MnO_2/CPCN, respectively, and the hierarchical structure of these models is consistent with the actual characterization results.

Fig. 4(a) exhibits the XRD patterns of CC, Co-MOFs@CC, CPCN@CC, MnO_2/CPCN@CC, Au/CPCN@CC, and Au-MnO_2/CPCN@CC. The peak at 25.74° is associated with carbon according to the standard card of JCPDS 15–0806, and those at 44.22°, 51.52° and 75.85° stem from the (111), (200), and (220) planes of cobalt metal, indicating that Co-MOFs is carbonized by annealing the MOFs precursor at a high temperature and in situ reduction of Co^{2+} to metallic cobalt [53]. The blue line in Fig. 4(a) represents CPCN@CC. It can be seen that there is only carbon peak but no Co peak, which indicates that CO-MOF nanosheets are transformed into pure porous carbon after nitric acid etching. The XRD patterns of the MnO_2/CPCN@CC, Au/CPCN@CC, and Au-MnO_2/CPCN@CC are shown in the green, purple, and yellow curves in Fig. 4(a), respectively. The peaks at 18.60°, 26.62°, and 36.57° from MnO_2/CPCN@CC and Au-MnO_2/CPCN@CC correspond to the (200), (201), and (210) planes of α-MnO_2 (JCPDS 42–1316) [54], respectively, and those at 38.18°, 44.39°, and 77.55° from Au/CPCN@CC and Au-MnO_2/CPCN@CC correspond to the (111), (200), and (210) planes of monolithic gold (JCPDS 04–0784), respectively.

Fig. 4(b) confirms the presence of C, O, Mn and Au in Au-MnO_2 /CPCN@CC. Fig. S2 shows the XPS spectrum of MnO_2/CPCN@CC, the built-in figure compares the Mn spectra of MnO_2 /CPCN@CC and Au-MnO_2 /CPCN@CC, and after the deposition of gold particles the Mn peak is red-shift from 641.1 eV and 652.9 to 640.9 eV and 652.5 eV, respectively. By comparing the carbon peak locations with those in the standard spectra, the carbon peak does not shift and remains at 285 eV. The Au 4 *f* binding energy peaks are at 83.93 eV and 87.60 eV as shown in Fig. 4(c) confirming the thin layer of AuNPs [55]. Fig. 4(d) shows peaks at 642.5 and 654.2 eV corresponding to Mn $2p^{3/2}$ and Mn $2p^{1/2}$ of MnO_2 and dominance of Mn^{4+} in the structure [56]. Fig. 4(e) shows that the O 1 *s* peak is mainly Mn-O bond at 529.4 eV and the peak at 531.2 eV arises from oxygen vacancies in MnO_2 [57–59]. Fig. S3 reveals that the Au-MnO_2/CPCN@CC electrode has a larger proportion of Mn and O compared to C, providing evidence of the uniform layer of MnO_2 on

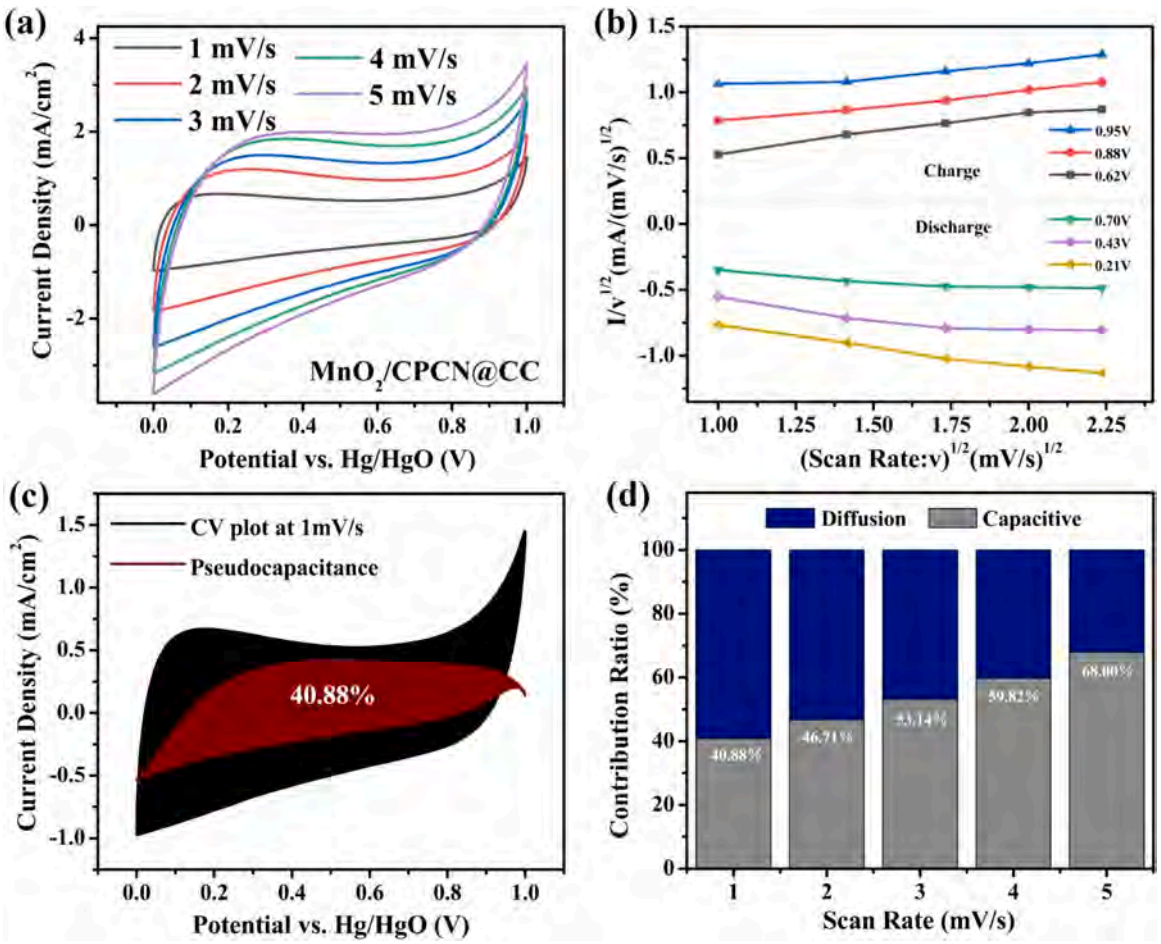

Fig. 7. Pseudocapacitance percentage analysis of the MnO_2/CPCN@CC electrode. (a) CV curves; (b) Current versus voltage in the CV curve; (c) Pseudocapacitance percentage analysis of the composite electrode at a scanning rate of 1 mV/s; (d) Pseudocapacitance percentage plot.

CPCN. The Brunauer-Emmet-Teller (BET) surface area is calculated from the N_2 adsorption-desorption isotherm data (Fig. 4(f)). The specific surface area of Au-MnO_2 @CC is 6.65 $m^2\ g^{-1}$, while the specific surface area of Au-MnO_2/CPCN@CC is 42.54 $m^2\ g^{-1}$.

The electrochemical results of CC, Co/CPCN@CC, CPCN@CC, Au/CPCN@CC, MnO_2/CPCN@CC, and Au-MnO_2/CPCN@CC are presented in Fig. 5. As shown in Fig. 5(a), the CV curves acquired at a scanning rate of 50 mV/s shows that Au-MnO_2/CPCN@CC has the largest closed interval area and superior electrical capacity. Fig. 5(b) shows the extensive discharging duration of Au-MnO_2/CPCN@CC further validating the pronounced specific capacitance. The Nyquist curves in Fig. 5(c) and Fig. S4 show that Au-MnO_2/CPCN@CC has a smaller semicircular arc in the high-frequency region indicative of fast charge transfer. Meanwhile, the curves in the low-frequency region are more vertical implying smaller diffusion impedance and enhanced ion transport [60,61]. The Au-MnO_2/CPCN@CC CV curves acquired at various scanning rates are displayed in Fig. 5(d). When the scanning rate goes up, the peak current becomes proportional to the square root of the scanning rate showing good electrochemical performance. The Faraday redox reaction for MnO_2 charge storage can be expressed as follows [62]:

$$MnO_2 + Na^+ + e^- \leftrightarrow MnOONa. \quad (5)$$

As seen in Fig. 5(e-f), Au-MnO_2/CPCN@CC is evaluated at different current densities (0.125–4 mA/cm^2). According to Eq. (1) and Table S1, the specific capacitances of the composite electrode are 503.72, 485.22, 393.19, 358.76, 352.36, and 351.71 F/g when the discharge current densities are 0.125, 0.25, 0.5, 1, 2, and 4 mA/cm^2, respectively. Fig. 5(d) shows that the charging curve is more symmetrical than the discharge curve, and the discharging current is inversely proportional to the discharging time thus showing good multiple Coulomb characteristics. The cycling stability is evaluated using 10,000 charging and discharging cycles at 4 mA/cm^2. The SEM images of Au-MnO_2/CPCN@CC after the cycles are shown in Fig. S5, part of the active material is shed after cycling, but the structure of porous carbon substrate is still stable, the capacitance retention rates of Au-MnO_2/CPCN@CC and MnO_2/CPCN@CC after cycling are 87.68% and 61.07%, respectively (Fig. 5(g)).

Fig. 5(h) presents the leakage current curve of Au-MnO_2/CPCN@CC when it is charged by a current of 2 mA at up to 1 V. The leakage current is then applied to maintain the electrode potential at 1 V [63]. The leakage current decreases swiftly to 0.034 mA in a short time and then remains stable for the next 2 h. The electrode shows a smaller leakage current (0.048 mA) in 1 M Na_2SO_4 than MnO_2/TiN@CC [44]. The low leakage current suggests less shuttle response caused by impurities in the materials or electrolyte [63], consequently allowing the supercapacitors to store charges more efficiently and maintain a stable voltage output. Fig. 5(i) displays the self-discharge behavior of Au-MnO_2/CPCN@CC. The electrode potential decreases gradually with time due to the leakage current. The discharging rate is most significant in the first 2 h of discharge and then stabilizes subsequently. The electrode potential maintains a stable output potential of 771 mV after discharging for 5 h and the potential of approximately 743 mV after 24 h is superior to that demonstrated previously [43,44].

Fig. 6 presents the pseudocapacitance percentage of the Au-MnO_2/CPCN@CC electrode calculated from the CV plot in Fig. 6(a) by Eq. (6) [64]:

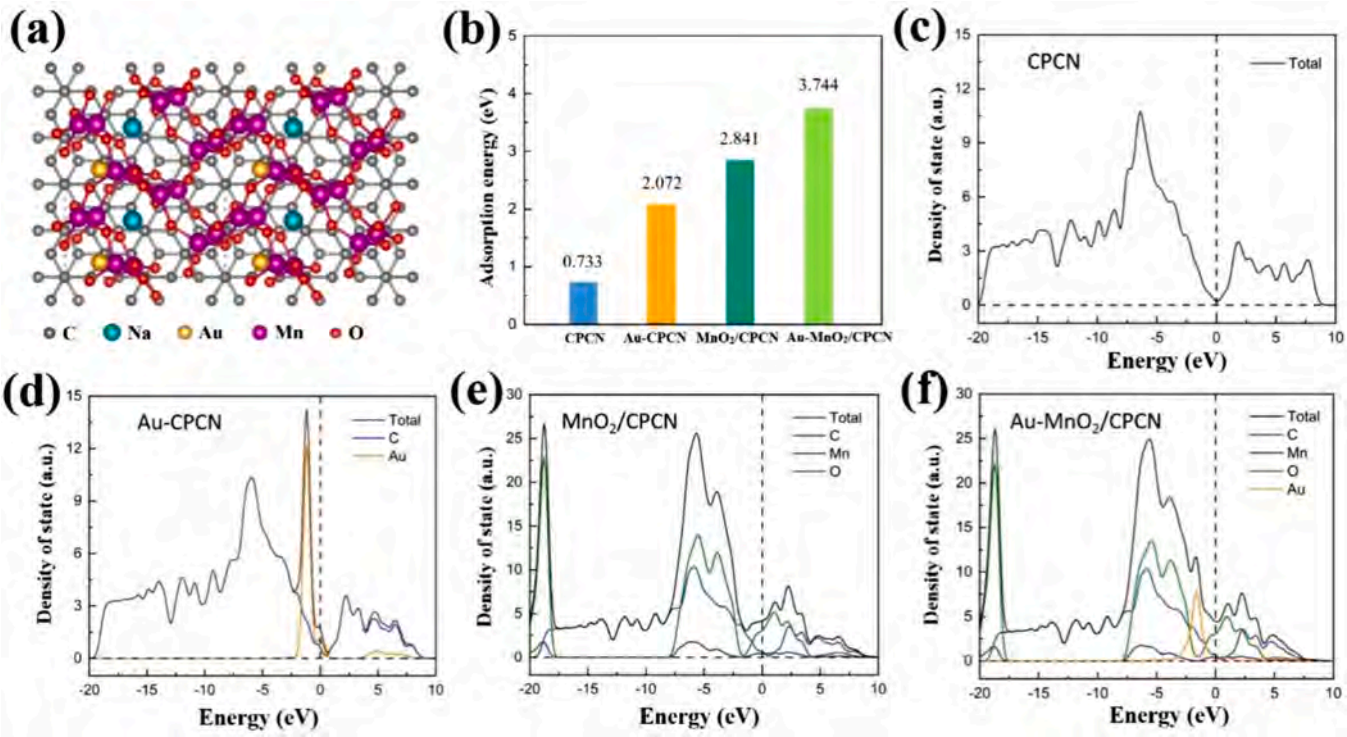

Fig. 8. (a) The top-view atomic structure of Au-MnO_2/CPCN; (b) Adsorption energies of CPCN, Au-CPCN, MnO_2/CPCN, and Au-MnO_2/CPCN; Density of states (DOS): (c) CPCN, (d) Au-CPCN, (e) MnO_2/CPCN, and (f) Au-MnO_2/CPCN. The vertical dashed lines in (c-f) at zero energy represent the Fermi levels.

$$i(V)/v^{1/2} = k_1 v^{1/2} + k_2, \tag{6}$$

where v(V/s) is the scanning rate and i(V) is the current corresponding to a randomly selected voltage (V) in the CV curve. The slope of the line in Fig. 6(b) is k_1 and k_2 is a constant. The current in the pseudocapacitor at different potentials is determined by k_1. With k_1 as the vertical coordinate and corresponding voltage (V) as the horizontal coordinate, the red dots are marked at the corresponding locations in Fig. 6(c). The red region composed of many different potentials is the pseudocapacitance of the active materials, and Fig. 6(d) summarizes the proportion of the contributed pseudocapacitance at various scanning rates according to this method. At a scanning rate of 1 mV/s, the pseudocapacitance percentage derived by CV is 83.80% and at a scanning rate of 5 mV/s scan rate, the pseudocapacitance percentage is 92.16%, indicative of pseudocapacitance characteristics.

The pseudocapacitances of MnO_2/CPCN@CC and Au/CPCN@CC can be obtained from Fig. 7 and Fig. S6 by using the same method as the MnO_2 composite electrode. According to Fig. 7(c) and Fig. S6(c), 78.43% and 40.88% of the CV surface capacitances are contributed to the Faraday capacitance, which is lower than that of the AuNPs-covered electrode under the same conditions. Fig. 7(d) and Fig. S6(d) summarize the percentage of pseudocapacitance contributions of MnO_2/CPCN@CC and Au/CPCN@CC at each scanning rate. By comparing Fig. 6(d), Fig. 7(d), and Fig. S6(d), the pseudo-capacitive contribution of Au-MnO_2/CPCN@CC is bigger.

In order to elucidate the underlying mechanism why gold particles improve the properties of the electrode materials, density-functional theory (DFT) calculations are performed using four computational models of rectangular parallelepipeds as shown in the side view of Fig. 3(f-i) and the top view of Fig. 8(a) and Fig. S7-S9. The sodium ion adsorption ability and DOS values are determined. The adsorption energies E_{ad} of sodium ions on CPCN, Au/CPCN, MnO_2/CPCN, and Au-MnO_2/CPCN are defined by the following formula:

$$E_{ad} = E_{sub} + E_{ion} - E_{tot}, \tag{7}$$

where E_{tot} is the total energy of the substrate with adsorbed ions, E_{sub} is the energy of CPCN, Au-CPCN, MnO_2/CPCN and Au-MnO_2/CPCN, respectively, and E_{ion} is the energy of isolated sodium ions. Accordingly, a positive value indicates an exothermic reaction and the larger the positive value, the more favorable sodium ion adsorption on the substrate. The calculated adsorption energies of sodium ions on CPCN, Au/CPCN, MnO_2/CPCN, and Au-MnO_2/CPCN are 0.733 eV, 2.072 eV, 2.841 eV, and 3.744 eV, respectively, as shown in Fig. 8(b). Hence, Au-MnO_2/CPCN is the best with respect to adsorption of sodium ions consistent with the experimental results. In order to compare the conductive properties of the substrates of CPCN, Au/CPCN, MnO_2/CPCN and Au-MnO_2/CPCN, the density of states (DOS) is derived and shown in Fig. 8(c-f). By comparing the DOS near the Fermi levels, Au-MnO_2/CPCN has better conductivity.

Eq. (3) shows that the energy density of a supercapacitor increases quadratically with the operating voltage. Therefore, a higher operating voltage leads to a larger energy density in the supercapacitor. A hybrid asymmetric supercapacitor (ASC) is fabricated and encapsulated in a button cell with CC, CPCN@CC, Au/CPCN@CC, MnO_2/CPCN@CC, or Au-MnO_2/CPCN@CC as the anode, AC@CC as the cathode, and $NaPF_6$ as the electrolyte for a high operating voltage of 4.0 V. The sodium-ion supercapacitors are designated as CC//AC@CC, CPCN@CC//AC@CC, ACPCN@CC//AC@CC, MCPCN@CC//AC@CC, and AMCPCN@CC//AC@CC, respectively. According to Fig. 9(a), AMCPCN@CC//AC@CC exhibits no significant distortion in the voltage window of 0–4.0 V. The GCD curves in Fig. 9(b) demonstrate that AMCPCN@CC//AC@CC has good multiplicative characteristics for different cutoff voltages up to 4.0 V. Fig. 8(c) shows that AMCPCN@CC//AC@CC can withstand high scan rates above 2400 mV/s while retaining a rectangular CV curve. As shown by the charging and discharging curves in Fig. 9(d), this device has good Coulombic efficiency and multiplicity characteristics. A higher operating voltage further increases the energy densities and power. The energy densities and power are calculated based on the discharging time in the GCD curve and Eqs. (3) and (4). The power densities of AMCPCN@CC//AC@CC at 71.48, 71.24, 61.46, 52.9, 42.34, 28.00, and

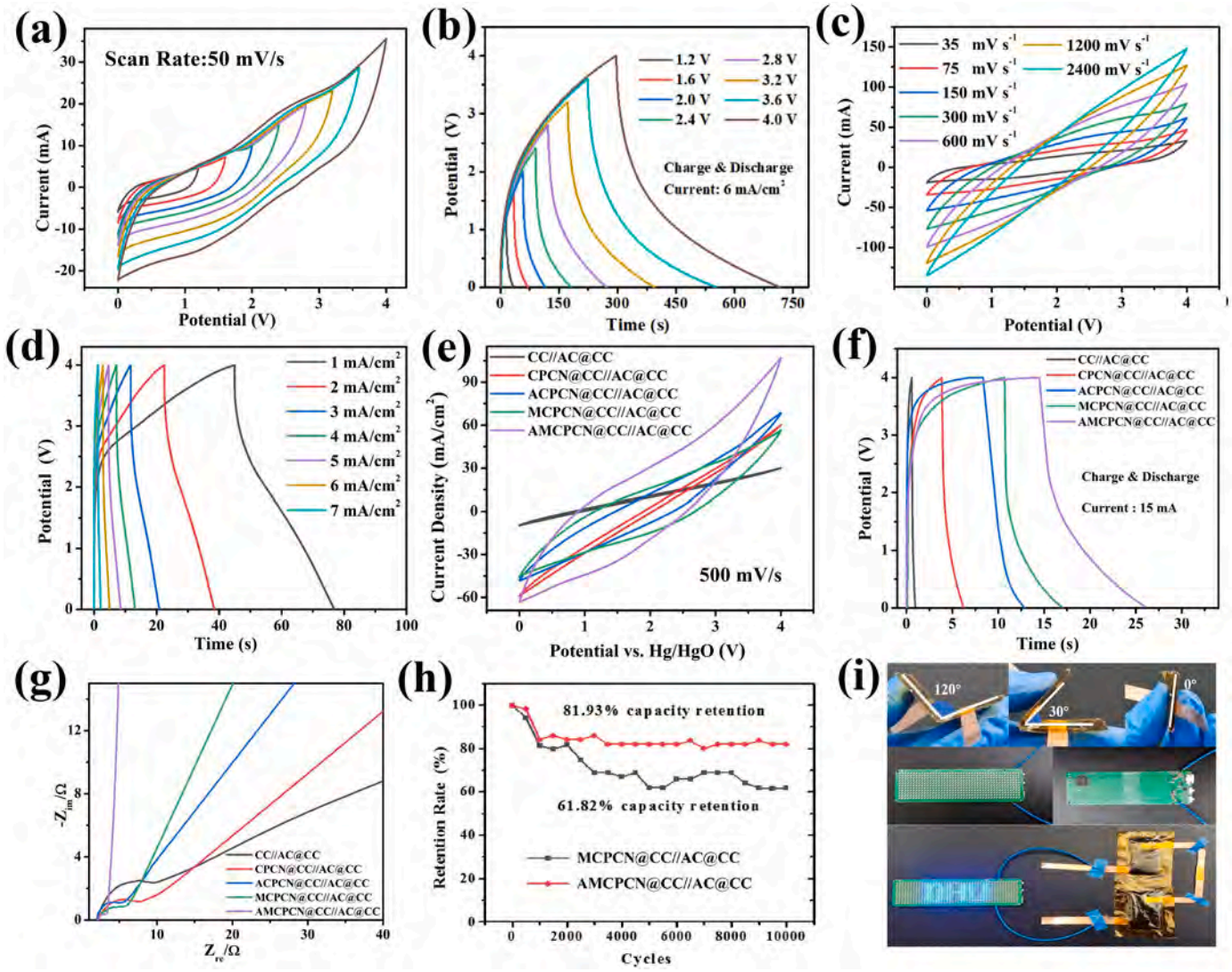

Fig. 9. Electrochemical properties of the hybrid supercapacitor consisting of the the composite electrode as the anode in the AMCPCN@CC//AC@CC supercapacitor: (a) CV peaks in different operating voltage windows; (b) GCD step curves at different cutoff voltages; (c) CV curves at different scanning rates; (d) GCD curves at different current densities; (e) CV curves, (f) GCD curves and (g) EIS curves of the series of composite supercapacitors; (h) Comparison of the cycling stability of AMCPCN@CC//AC@CC and MCPCN@CC//AC@CC; (i) FASC showing multiple angle bending and connecting two FASCs in parallel to power the LED array.

Table 1
The electrochemical characteristic of different devices based on MnO_2 electrodes.

Electrodes	Potential Window (V)	Specific Capacitance (F g^{-1})	Energy Density (Wh kg^{-1})	Power Density (W kg^{-1})	Retention Rate	Refs
$NiCo_2O_4$@MnO_2//AC	1.5	—	37.8	187.5	98.38%@3000cycles	[65]
MnO_2// Fe_2O_3@PPy	1.8 V	38.1	42.4	268.8	97.1%@3000cycles	[66]
AC//Co_3O_4@PPy@MnO_2	1.6 V	—	34.3	80	100.4%@11000cycles	[67]
MnO_2//AG	0.8 V	365	22.5	146.2	90.4%@3000 cycles	[68]
MnO_2/CNT//AC	2 V	60	27	225	—	[69]
AMCPCN@CC//AC@CC	4 V	503.72	52.9	320	81.93%@10000 cycles	this work

13.52 Wh/kg energy densities correspond to 79.96, 159.96, 239.96, 320.00, 400.04, 480.00, and 559.60 W/kg power densities, respectively, which is higher than previous reported in Table 1.

According to Fig. 9(e), the AMCPCN@CC//AC@CC electrode shows the largest region in the closed interval of the CV curve at the same scanning rate thereby showing the highest capacity. Consistent with CV, Fig. 9(f) shows that AMCPCN@CC//AC@CC has the longest discharging time and greater specific capacitance. Fig. 9(g) shows the Nyquist curves of the ACs. The smaller semicircular arc of AMCPCN@CC//AC@CC in the peak frequency region (Fig. S10) and more vertical curve in the low-frequency area compared with other electrodes suggest better characteristics. Fig. 9(h) shows that after 10,000 cycles, the AMCPCN@CC//AC@CC supercapacitor retains 81.93% of the capacitance compared to 61.82% observed from MCPCN@CC//AC@CC. The change may arise from more contact with the electrolyte and more active materials. However, after cycling, the structure collapses or dissolves in the electrolyte, resulting in lost electrode capacity. To confirm the practical feasibility of sodium-ion supercapacitors, a flexible asymmetric

supercapacitor (FASC) is assembled with Au-MnO_2/CPCN@CC as the anode, AC@CC as the cathode, and $NaPF_6$ as the electrolyte. Fig. 8(i) shows high tolerance to mechanical banding and two flexible devices connected in series can power the LED array after charging for 10 s at a high current. The results show that the fast-charging and flexible supercapacitor with a wide voltage window has large potential in energy storage applications.

4. Conclusion

The Au-MnO_2/CPCN@CC electrode is designed and demonstrated for asymmetric supercapacitors (ASCs). It is synthesized by incorporating manganese dioxide nanoparticles into a porous carbon skeleton on a piece of conductive carbon cloth in conjunction with deposition of AuNPs. After MOFs etching, the porous carbon skeleton has a large surface area and the AuNPs increase the electrical conductivity. The electrochemical properties of the Au-MnO_2/CPCN@CC electrode is improved significantly by AuNPs deposition. After 10,000 cycles at a current density of 4 mA/cm^2, the capacitance retention rate is 87.68%. The small loss confirms the good electrochemical stability and high specific capacitance. Density-functional theory (DFT) calculations reveal a sodium ion adsorption energy of 3.744 eV and large DOS value near the Fermi level. To demonstrate the practical feasibility, Au-MnO_2/CPCN@CC and AC@CC are incorporated into an asymmetric supercapacitor as the positive electrode and negative electrode, and in the 4 V window, the device can endure a high scanning rate of 2400 mV/s. Hence, the Au-MnO_2/CPCN@CC electrode has large potential in energy storage devices and our results also provide insights into the preparation and surface modification of metal hydroxide ASCs.

Declaration of Competing Interest

We have no competing interests, including but not limited to employment, consultancy, patents, honoraria, or ownership of stocks or shares in any organization that may influence our research in any way.

Data availability

Data will be made available on request.

Acknowledgments

The research was funded by the National Natural Science Foundation of China (grant number 22005046), City University of Hong Kong Donation Research Grants (grant numbers DON-RMG 9229021 and 9220061) and Strategic Research Grant of City University of Hong Kong (SRG) (grant number 7005505).

Appendix A. Supporting information

Supplementary data associated with this article can be found in the online version at doi:10.1016/j.jallcom.2023.172431.

References

[1] M. Su, Z. Pan, Y. Chong, C. Ye, X. Jin, Q. Wu, Z. Hu, D. Ye, G.I.N. Waterhouse, Y. Qiu, S. Yang, Boosting the electrochemical performance of hematite nanorods via quenching-induced metal single atom functionalization, J. Mater. Chem. A 9 (2021) 3492–3499.
[2] G. He, D. Wang, H. HuangFu, C. Zhang, B. Zhang, Y. Mi, D. Zheng, Bifunctional modulation of Ce^{4+} doping for $ZnWO_4$ morphological structure and bandgap width to enhance photocatalytic, Degrad. Electrochem. Energy Storage, J. Mater. Sci. 57 (2022) 13541–13559.
[3] N. Chakrabarty, A. Dey, S. Krishnamurthy, A.K. Chakraborty, CeO_2/Ce_2O_3 quantum dot decorated reduced graphene oxide nanohybrid as electrode for supercapacitor, J. Appl. Surf. Sci. 536 (2021), 147960.
[4] Y. Sun, S. Liu, N. Huang, X. Wang, J. Liu, J. Bi, J. Zhang, L. Guo, X. Sun, Regulation of preferred crystal plane and oxygen vacancy of $CoWO_4$ with morphology remodeling to boost electrochemical performances for battery-supercapacitor hybrid device electrode, J. Power Sources 545 (2022), 231911.
[5] Q. Wang, T. Zhong, Z. Wang, Plasma-engineered N-CoO_x nanowire array as a bifunctional electrode for supercapacitor and electrocatalysis, Nanomaterials 12 (2022) 2984.
[6] Y. Wang, T. Zhang, J. Xiao, X. Tian, S. Yuan, Enhancing electrochemical performance of ultrasmall Fe_2O_3-embedded carbon nanotubes via combusting-induced high-valence dopants, J. Mater. Sci. Technol. 134 (2023) 142–150.
[7] S. Kumar, G. Saeed, L. Zhu, K.N. Hui, N.H. Kim, J.H. Lee, 0D to 3D carbon-based networks combined with pseudocapacitive electrode material for high energy density supercapacitor: a review, Chem. Eng. J. 403 (2021), 126352.
[8] R. Sha, P.C. Maity, U. Rajaji, T.-Y. Liu, T.K. Bhattacharyya, Review—$MoSe_2$ nanostructures and related electrodes for advanced supercapacitor developments, J. Electrochem. Soc. 169 (2022), 013503.
[9] E. Frackowiak, Carbon materials for supercapacitor, Appl., J. Phys. Chem. C 111 (2007) 1774–1785.
[10] Z.S. Iro, A. Brief, Review on electrode materials for supercapacitor, Int. J. Electrochem. Sci. 11 (2016) 10628–10643.
[11] D. Nandi, V.B. Mohan, A.K. Bhowmick, D. Bhattacharyya, Metal/metal oxide decorated graphene synthesis and application as supercapacitor: a review, J. Mater. Sci. 55 (2020) 6375–6400.
[12] M. Kandasamy, S. Sahoo, S.K. Nayak, B. Chakraborty, C.S. Rout, Recent advances in engineered metal oxide nanostructures for supercapacitor applications: experimental and theoretical aspects, J. Mater. Chem. A 9 (2021) 17643–17700.
[13] Q. Meng, K. Cai, Y. Chen, L. Chen, Research progress on conducting polymer-based supercapacitor electrode materials, Nano Energy 36 (2017) 268–285.
[14] P. Naskar, A. Maiti, P. Chakraborty, D. Kundu, B. Biswas, A. Banerjee, Chemical supercapacitors: a review focusing on metallic compounds and conducting polymers, J. Mater. Chem. A 9 (2021) 1970–2017.
[15] K. Gao, Z. Zheng, Z. Feng, Q. Niu, Q. Tang, X. Sun, L. Wang, Nanofiber-based nitrogen-doped carbon aerogel film for flexible solid supercapacitors, J. Electron. Mater. 52 (2022) 1121–1131.
[16] R. Sha, S. Badhulika, Binder free platinum nanoparticles decorated graphene-polyaniline composite film for high performance supercapacitor application, Electrochim. Acta 251 (2017) 505–512.
[17] H. Wang, H. Niu, H. Wang, W. Wang, X. Jin, H. Wang, H. Zhou, T. Lin, Micro-meso porous structured carbon nanofibers with ultra-high surface area and large supercapacitor electrode capacitance, J. Power Sources 482 (2021), 228986.
[18] Y. Wang, L. Zhang, H. Hou, W. Xu, G. Duan, S. He, K. Liu, S. Jiang, Recent progress in carbon-based materials for supercapacitor electrodes: a review, J. Mater. Sci. 56 (2020) 173–200.
[19] J. Yin, W. Zhang, N.A. Alhebshi, N. Salah, H.N. Alshareef, Synthesis strategies of porous carbon for supercapacitor applications, Small Methods 4 (2020) 1900853.
[20] J. Chen, X. Zhou, M. Zhang, J. Wang, H. Li, J. Wang, C. Wang, Designing of carbon cloth@Co-MOF@SiO_2 as superior flexible anode for lithium-ion battery, J. Alloy. Compd. 902 (2022), 163680.
[21] M.R. Rosario-Canales, P. Deria, M.J. Therien, J.J. Santiago-Aviles, Composite electronic materials based on poly(3,4-propylenedioxythiophene) and highly charged poly(aryleneethynylene)-wrapped carbon nanotubes for supercapacitors, ACS Appl. Mater. Inter. 4 (2012) 102–109.
[22] N.L. Torad, R.R. Salunkhe, Y. Li, H. Hamoudi, M. Imura, Y. Sakka, C.C. Hu, Y. Yamauchi, Y. electric double-layer capacitors based on highly graphitized nanoporous carbons derived from ZIF-67, Chem. Eur. J. 20 (2014) 7895–7900.
[23] D. Van Lam, M. Sohail, J.-H. Kim, H.J. Lee, S.O. Han, J. Shin, D. Kim, H. Kim, S.-M. Lee, Laser synthesis of MOF-derived Ni@carbon for high-performance pseudocapacitors, ACS Appl. Mater. Interfaces12 (2020) 39154–39162.
[24] J. Wang, X. Luo, C. Young, J. Kim, Y.V. Kaneti, J. You, Y.-M. Kang, Y. Yamauchi, K. C.W. Wu, A. Glucose-Assisted, Hydrothermal reaction for directly transforming metal–organic frameworks into hollow carbonaceous materials, Chem. Mater. 30 (2018) 4401–4408.
[25] J. Pokharel, A. Gurung, A. Baniya, W. He, K. Chen, R. Pathak, B.S. Lamsal, N. Ghimire, Y. Zhou, MOF-derived hierarchical carbon network as an extremely-high-performance supercapacitor electrode, Electrochim. Acta 394 (2021) 139058.
[26] C.-H. Wang, D.-W. Zhang, S. Liu, Y. Yamauchi, F.-B. Zhang, Y.V. Kaneti, Ultrathin nanosheet-assembled nickel-based metal–organic framework microflowers for supercapacitor applications, ChemComm 58 (2022) 1009–1012.
[27] R. Sha, A. Gopalakrishnan, K.V. Sreenivasulu, V.V.S.S. Srikanth, S. Badhulika, Template-cum-catalysis free synthesis of α-MnO_2 nanorods-hierarchical MoS_2 microspheres composite for ultra-sensitive and selective determination of nitrite, J. Alloy. Compd. 794 (2019) 26–34.
[28] A.H. Reaz, S. Saha, C.K. Roy, M.A. Wahab, G. Will, M.A. Amin, Y. Yamauchi, S. Liu, Y.V. Kaneti, M.S. Hossain, S.H. Firoz, Boosting capacitive performance of manganese oxide nanorods by decorating with three-dimensional crushed graphene, Nano Converg. 9 (2022) 10.
[29] N. Vangapally, K.K. V, A. Kumar, S.K. Martha, Charge storage behavior of sugar derived carbon/MnO_2 composite electrode material for high-performance supercapacitors, J. Alloy. Compd. 893 (2022), 162232.
[30] L. Lian, J. Yang, P. Xiong, W. Zhang, M. Wei, Facile synthesis of hierarchical MnO_2 sub-microspheres composed of nanosheets and their application for supercapacitors, RSC Adv. 4 (2014) 40753–40757.
[31] X. Lu, M. Yu, G. Wang, T. Zhai, S. Xie, Y. Ling, Y. Tong, Y. Li, H-TiO_2@MnO_2//H-TiO_2@C core-shell nanowires for high performance and flexible asymmetric supercapacitors, Adv. Mater. 25 (2013) 267–272.
[32] P.Y. Tang, Y.Q. Zhao, Y.M. Wang, C.L. Xu, A metal-decorated nickel foam-inducing regulatable manganese dioxide nanosheet array architecture for high-performance supercapacitor applications, Nanoscale 5 (2013) 8156–8163.

[33] W. Liu, Z. Wang, Y. Su, Q. Li, Z. Zhao, F. Geng, Molecularly stacking manganese dioxide/titanium carbide sheets to produce highly flexible and conductive film electrodes with improved pseudocapacitive performances, Adv. Energy Mater. 7 (2017) 1602834.
[34] P. Ning, X. Duan, X. Ju, X. Lin, X. Tong, X. Pan, T. Wang, Q. Li, Facile synthesis of carbon nanofibers/MnO_2 nanosheets as high-performance electrodes for asymmetric supercapacitors, Electrochim. Acta 210 (2016) 754–761.
[35] C. Wu, Y. Zhu, M. Ding, C. Jia, K. Zhang, Fabrication of plate-like MnO_2 with excellent cycle stability for supercapacitor electrodes, Electrochim. Acta 291 (2018) 249–255.
[36] K. Xu, S. Li, J. Yang, J. Hu, Hierarchical hollow MnO_2 nanofibers with enhanced supercapacitor performance, J. Colloid Interface Sci. 513 (2018) 448–454.
[37] Z. Hu, X. Xiao, C. Chen, T. Li, L. Huang, C. Zhang, J. Su, L. Miao, J. Jiang, Y. Zhang, J. J. Zhou, Al-doped α-MnO_2 for high mass-loading pseudocapacitor with excellent cycling stability, Nano Energy 11 (2015) 226–234.
[38] J. Yang, L. Lian, H. Ruan, F. Xie, M. Wei, Nanostructured porous MnO_2 on Ni foam substrate with a high mass loading via a CV electrodeposition route for supercapacitor application, Electrochim. Acta 136 (2014) 189–194.
[39] A. Eftekhari, L. Li, Y. Yang, Polyaniline supercapacitors, J. Power Sources 347 (2017) 86–107.
[40] J. Cao, M. Safdar, Z. Wang, J. He, High-performance flexible supercapacitor electrodes based on Te nanowire arrays, J. Mater. Chem. A 1 (2013) 10024–10029.
[41] Z. Çıplak, N. Yıldız, Polyaniline-Au nanocomposite as electrode material for supercapacitor applications, Synth. Met. 256 (2019), 116150.
[42] L. Khandare, S. Terdale, Gold nanoparticles decorated MnO_2 nanowires for high performance supercapacitor, Appl. Surf. Sci. 418 (2017) 22–29.
[43] M. Li, K. Zhu, H. Zhao, Z. Meng, C. Wang, P.K. Chu, Construction of α-MnO_2 on carbon fibers modified with carbon nanotubes for ultrafast flexible supercapacitors in ionic liquid electrolytes with wide voltage windows, Nanomaterials 12 (2022) 2020.
[44] M. Li, K. Zhu, Z. Meng, R. Hu, J. Wang, C. Wang, P.K. Chu, Efficient coupling of MnO_2/TiN on carbon cloth positive electrode and Fe_2O_3/TiN on carbon cloth negative electrode for flexible ultra-fast hybrid supercapacitors, RSC Adv. 11 (2021) 35726–35736.
[45] X. Yang, Y. Li, P. Zhang, L. Sun, X. Ren, H. Mi, Hierarchical hollow carbon spheres: novel synthesis strategy, pore structure engineering and application for micro-supercapacitor, Carbon 157 (2020) 70–79.
[46] J.-G. Wang, Y. Yang, Z.H. Huang, F. Kang, A high-performance asymmetric supercapacitor based on carbon and carbon–MnO_2 nanofiber electrodes, Carbon 61 (2013) 190–199.
[47] Z. Shang, X. An, H. Zhang, M. Shen, F. Baker, Y. Liu, L. Liu, J. Yang, H. Cao, Q. Xu, H. Liu, Y. Ni, Houttuynia-derived nitrogen-doped hierarchically porous carbon for high-performance supercapacitor, Carbon 161 (2020) 62–70.
[48] K. Wang, Y. Chen, R. Tian, H. Li, Y. Zhou, H. Duan, H. Liu, Porous Co-C core-shell nanocomposites derived from Co-MOF-74 with enhanced electromagnetic wave absorption performance, ACS Appl. Mater. Inter. 10 (2018) 11333–11342.
[49] G. Kresse, J. Furthmüller, Efficiency of ab-initio total energy calculations for metals and semiconductors using a plane-wave basis set, Comput. Mater. Sci. 6 (1996) 15.
[50] G. Kresse, J. Furthmüller, Efficient iterative schemes for ab initio total-energy calculations using a plane-wave basis set, Phys. Rev. B 54 (1996) 11169.
[51] G. Kresse, D. Joubert, From ultrasoft pseudopotentials to the projector augmented-wave method, Phys. Rev. B 59 (1999) 1758.
[52] J.P. Perdew, K. Burke, M. Ernzerhof, Generalized gradient approximation made simple, Phys. Rev. Lett. 77 (1996) 3865.
[53] H.J. Monkhorst, J.D. Pack, Special points for Brillouin-zone integrations, Phys. Rev. B 13 (1976) 5188.
[54] H. Yang, X. Tang, L. Bai, L. Yang, J. Ding, R. Chen, X. Du, G. Li, H. Liang, Synergistic effects of prokaryotes and oxidants in rapid sand filters treatment of groundwater versus surface water: purification efficacy, stability and associated mechanisms, Chemosphere 295 (2022), 133804.
[55] C. Li, J. Balamurugan, D.C. Nguyen, N.H. Kim, J.H. Lee, Hierarchical manganese–nickel sulfide nanosheet arrays as an advanced electrode for all-solid-state asymmetric supercapacitors, ACS Appl. Mater. Inter. 12 (2020) 21505–21514.
[56] J. Lu, F. Lian, L. Guan, Y. Zhang, F. Ding, Adapting FeS_2 micron particles as an electrode material for lithium-ion batteries via simultaneous construction of CNT internal networks and external cages, J. Mater. Chem. A 7 (2019) 991–997.
[57] J. Wang, X. Guo, R. Cui, H. Huang, B. Liu, Y. Li, D. Wang, D. Zhao, J. Dong, S. Li, B. Sun, MnO_2/porous carbon nanotube/MnO_2 nanocomposites for high-performance supercapacitor, ACS Appl. Nano Mater. 3 (2020) 11152–11159.
[58] P. Lv, Y.Y. Feng, Y. Li, W. Feng, Carbon fabric-aligned carbon nanotube/MnO_2/conducting polymers ternary composite electrodes with high utilization and mass loading of MnO_2 for super-capacitors, J. Power Sources 220 (2012) 160–168.
[59] J.W. Wang, Y. Chen, B.Z. Chen, Synthesis and control of high-performance MnO_2/carbon nanotubes nanocomposites for supercapacitors, J. Alloy. Compd. 688 (2016) 184–197.
[60] P. Gao, P. Metz, T. Hey, Y. Gong, D. Liu, D.D. Edwards, J.Y. Howe, R. Huang, S. T. Misture, The critical role of point defects in improving the specific capacitance of delta-MnO_2 nanosheets, Nat. Commun. 8 (2017) 14559.
[61] P. Gao, D. Liu, Facile synthesis of copper oxide nanostructures and their application in non-enzymatic hydrogen peroxide sensing, Sens. Actuators B Chem. 208 (2015) 346–354.
[62] A.A. Mohammed, C. Chen, Z. Zhu, Green and high-performance all-solid-state supercapacitors based on MnO_2/Faidherbia albida fruit shell-derived carbon sphere electrodes, J. Power Sources 417 (2019) 1–13.
[63] Y. Wang, Z. He, H. Guo, P. Huang, H. Zhang, Lin, Enhanced electrochemical supercapacitor performance with a three-dimensional porous boron-doped diamond film, N. J. Chem. 43 (2019) 18813–18822.
[64] Y. Tan, Y. Liu, L. Kong, L. Kang, F. Ran, Supercapacitor electrode of nano-Co_3O_4 decorated with gold nanoparticles via in-situ reduction method, J. Power Sources 363 (2017) 1–8.
[65] Y. Zhang, B. Wang, F. Liu, J. Cheng, X.-w Zhang, L. Zhang, Full synergistic contribution of electrodeposited three-dimensional $NiCo_2O_4$@MnO_2 nanosheet networks electrode for asymmetric supercapacitors, Nano Energy 27 (2016) 627–637.
[66] P.-Y. Tang, L.-J. Han, A. Genç, Y.-M. He, X. Zhang, L. Zhang, J.R. Galán-Mascarós, J.R. Morante, J. Arbiol, Synergistic effects in 3D honeycomb-like hematite nanoflakes/branched polypyrrole nanoleaves heterostructures as high-performance negative electrodes for asymmetric supercapacitors, Nano Energy 22 (2016) 189–201.
[67] L. Han, P. Tang, L. Zhang, Hierarchical Co_3O_4@PPy@MnO_2 core–shell–shell nanowire arrays for enhanced electrochemical energy storage, Nano Energy 7 (2014) 42–51.
[68] M. Huang, Y. Zhang, F. Li, L. Zhang, R.S. Ruoff, Z. Wen, Q. Liu, Self-assembly of mesoporous nanotubes assembled from interwoven ultrathin birnessite-type MnO_2 nanosheets for asymmetric supercapacitors, Sci. Rep. 4 (2014) 3878.
[69] D. Gueon, J.H. Moon, MnO_2 nanoflake-shelled carbon nanotube particles for high-performance supercapacitors, ACS Sustain. Chem. Eng. 5 (2017) 2445–2453.

Supporting information

α-MnO_2 Composite with Gold Nanoparticles on Carbon Cloth Modified with MOFs-Derived Porous Carbon for Flexible and Activity-Enhanced Sodium-Ion Supercapacitors

Hanxue Zhao[a‡], Kaishuai Yang[c‡], Kailan Zhu[a‡], Mai Li[a*], Wendong Xu[a], Waqar ul Hasan[a], Jiale Wang[a], Qinglin Deng[b*], Jun Yu[e], Zhongyi Sun[e], Paul K. Chu[d]

[a] College of Science, Donghua University, Shanghai 201620, China

[b] School of Physics and Materials Science, Guangzhou University, Guangzhou 510006, China

[c] School of Electronic and Information Engineering, Changshu Institute of Technology, Suzhou 215000, P. R. China

[d] Department of Physics, Department of Materials Science and Engineering, and Department of Biomedical Engineering, City University of Hong Kong, Tat Chee Avenue, Kowloon, Hong Kong, China

[e] Semiconductor New Materials Research and Development Center, SHANGHAI Q-TECH CO., LTD., Zhengxue Road, Yangpu District, Shanghai, China

* Corresponding author: E-mail: limai@dhu.edu.cn (M. Li), qldeng@gzhu.edu.cn (Q.L. Deng)

‡ These authors contributed equally to this work

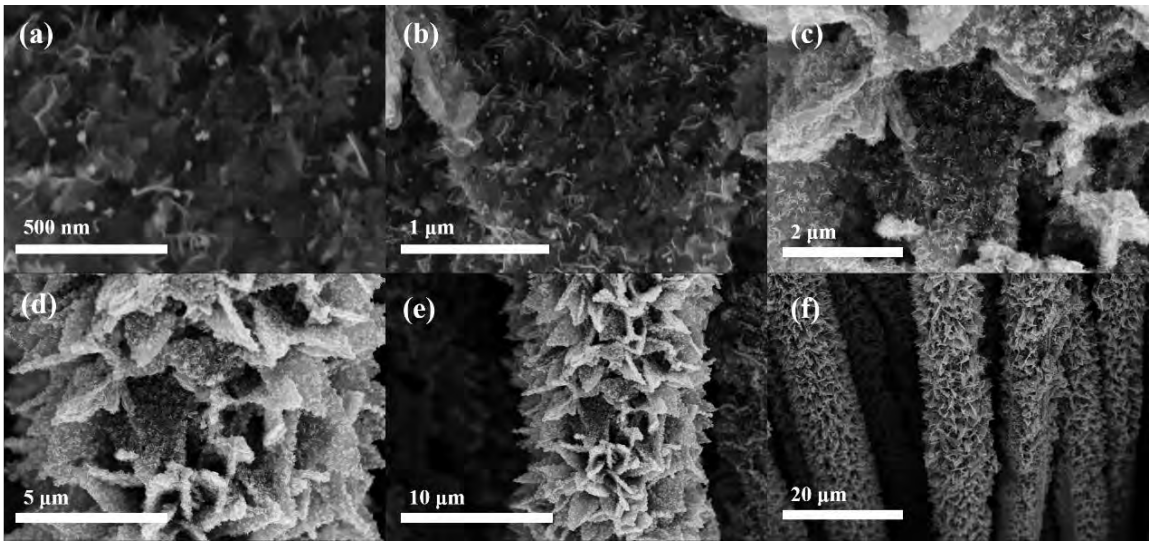

Fig. S1. SEM images of Au-MnO_2/CPCN@CC at different magnifications.

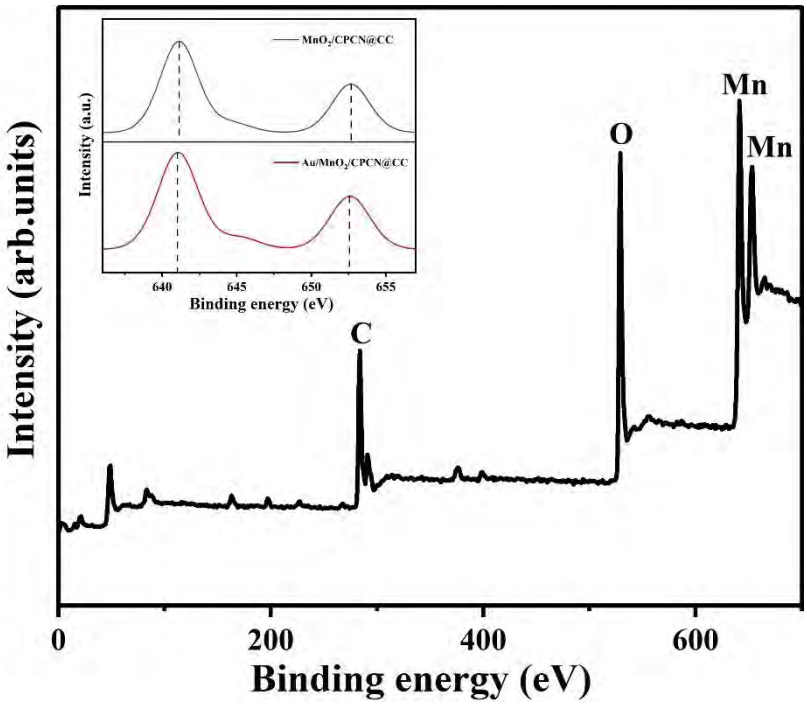

Fig. S2. The XPS spectrum of MnO_2/CPCN@CC

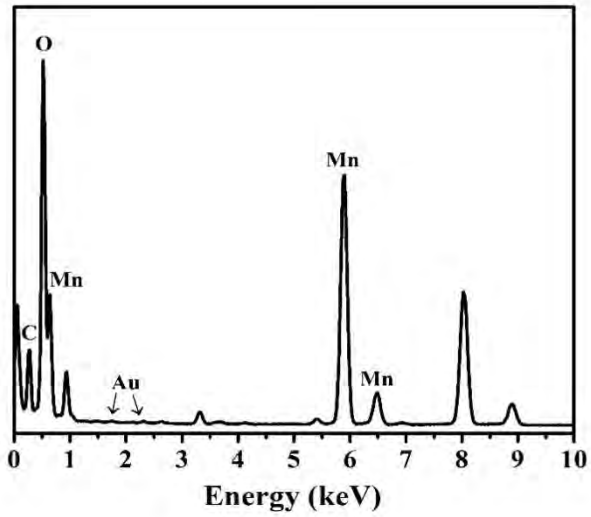

Fig. S3. EDS spectrum of Au-MnO_2/CPCN@CC

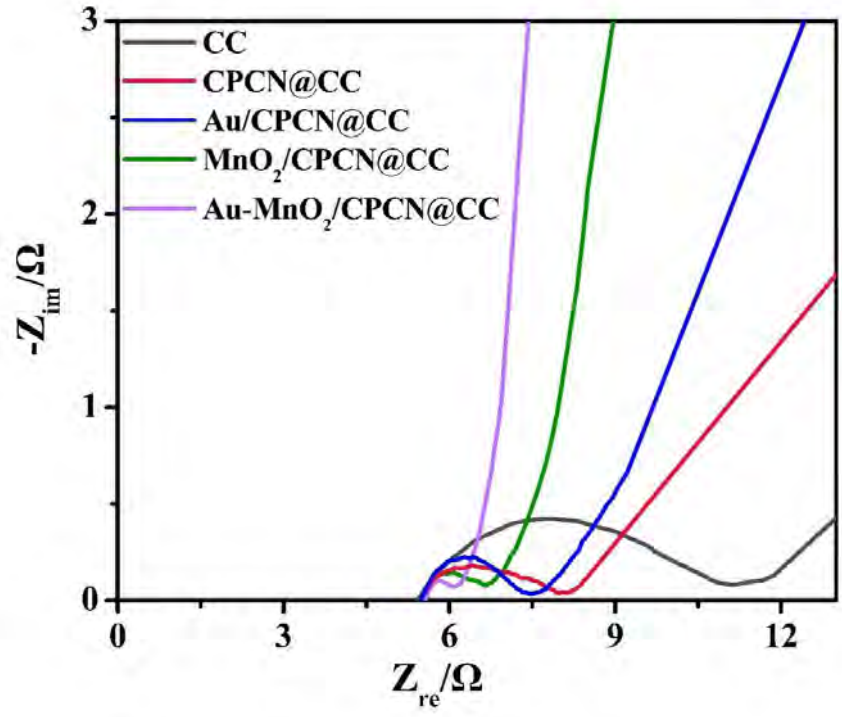

Fig. S4. High-frequency portion details of the EIS curves for CC, Co/CPCN@CC, CPCN@CC, Au/CPCN@CC, MnO_2/CPCN@CC, and Au-MnO_2/CPCN@CC.

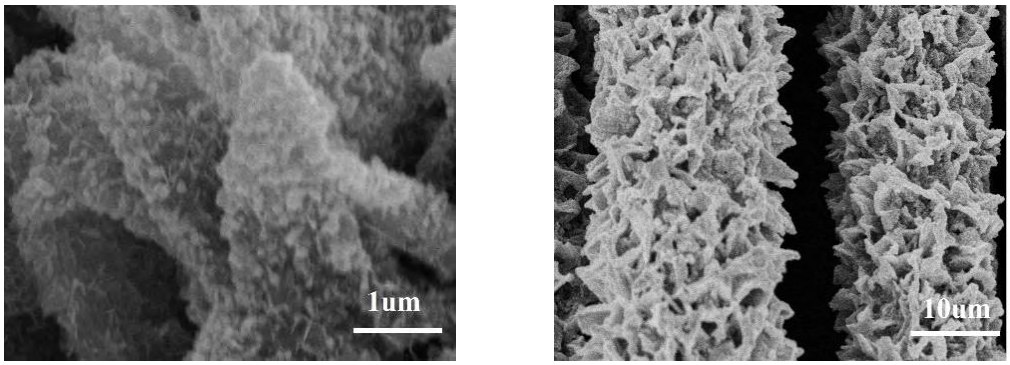

Fig. S5. The SEM images of Au-MnO_2/CPCN@CC after cycling.

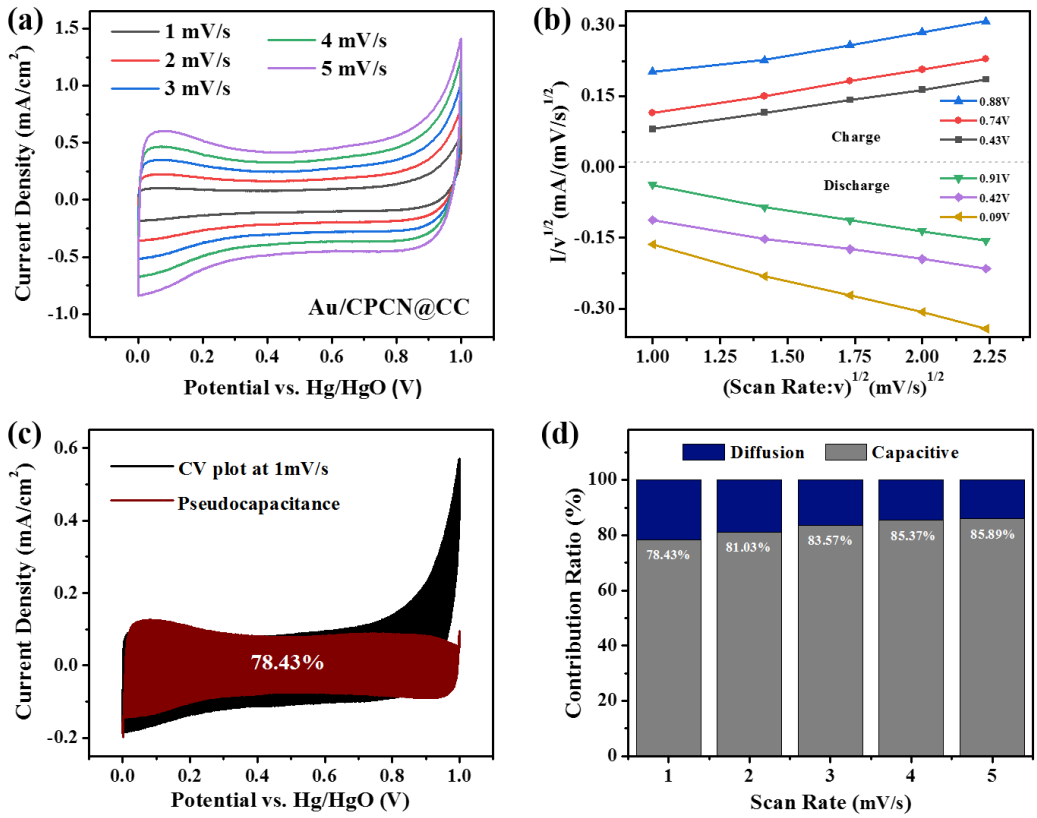

Fig. S6. Pseudocapacitance duty ratio analysis of Au/CPCN@CC electrode. (a) CV curves, (b) Plots of current versus voltage in CV curves, (c) Pseudocapacitance duty ratios of the composite electrode at a scanning rate of 1 mV/s, (d) Pseudocapacitance duty ratio plot.

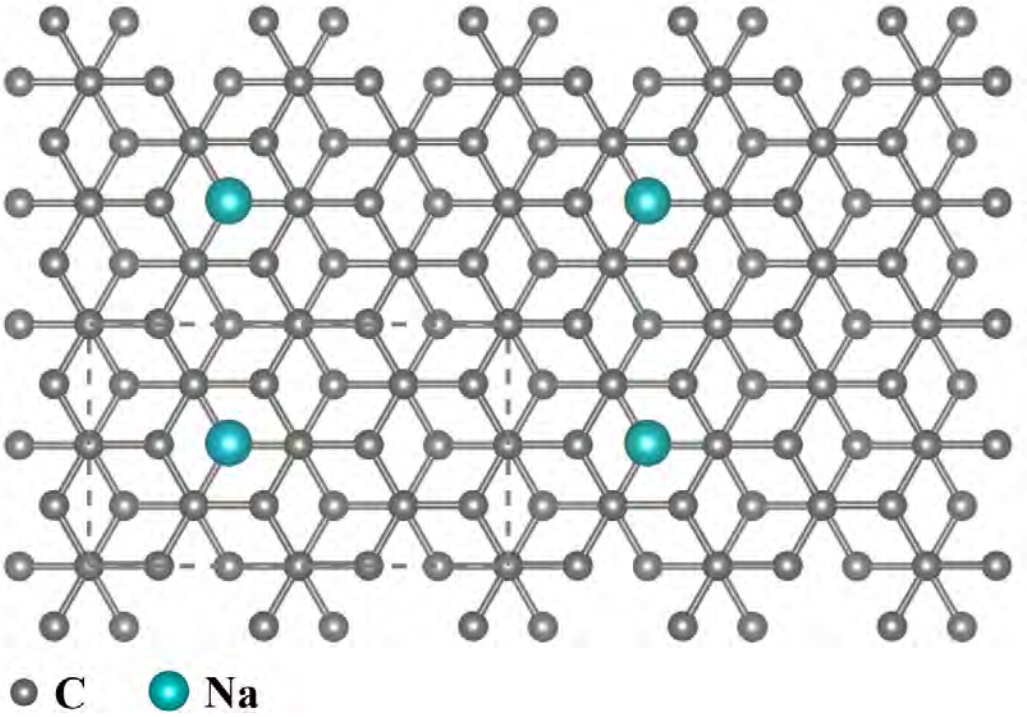

Fig.S7. The top-view atomic structure of CPCN.

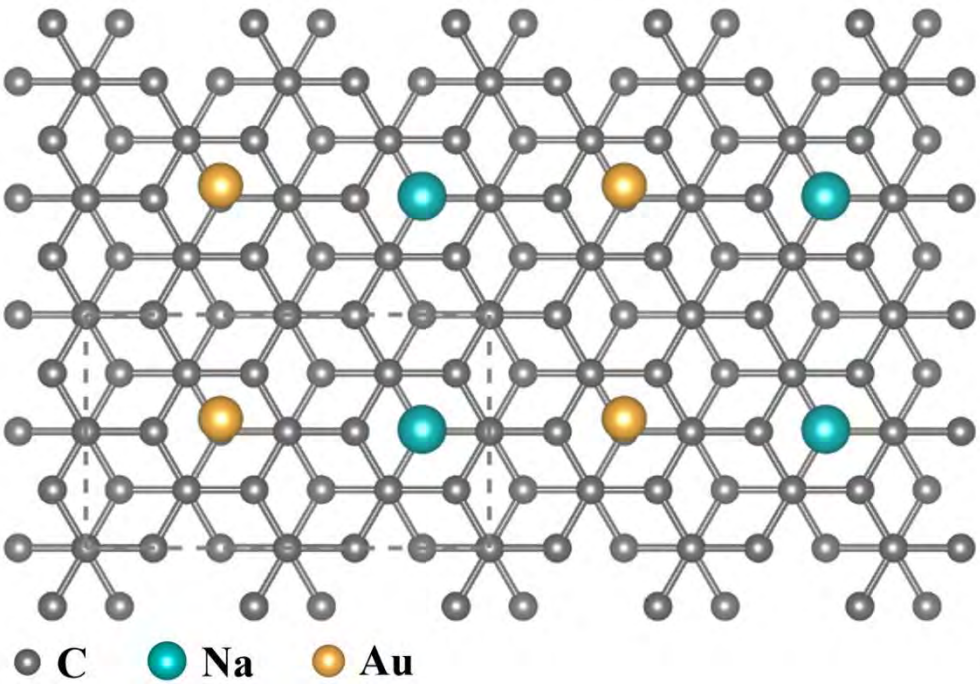

Fig.S8. The top-view atomic structure of Au-CPCN.

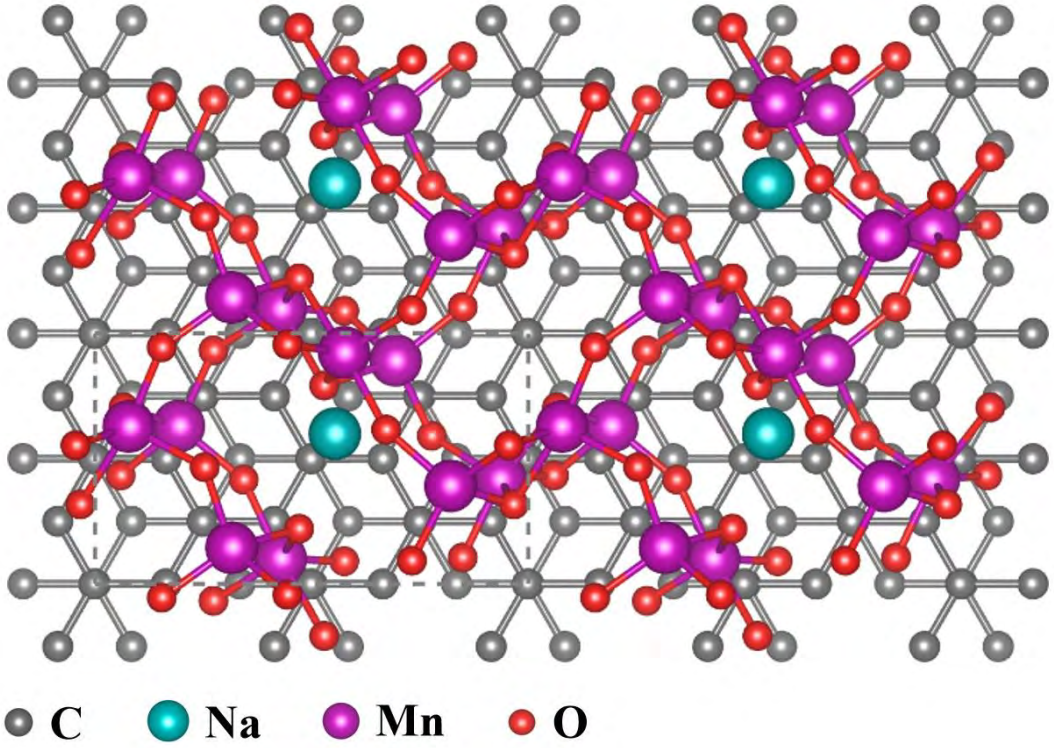

Fig.S9. The top-view atomic structure of MnO_2/CPCN.

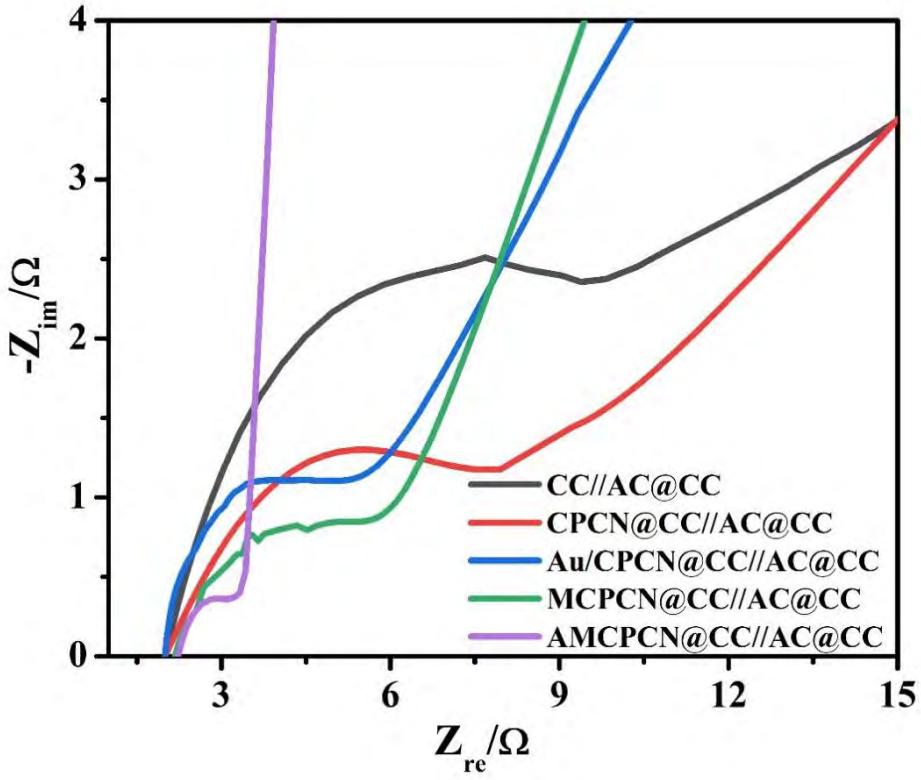

Fig. S10. High-frequency portion details of the EIS curves of the CC//AC@CC, CPCN@CC//AC@CC, ACPCN@CC//AC@CC, MCPCN@CC//AC@CC, and AMCPCN@CC//AC@CC supercapacitor.

Table S1. Specific capacitances of Au-MnO_2/CPCN@CC and MnO_2/CPCN@CC in 1 M Na_2SO_4.

Current Densities (Ma/cm^2)	**Specific Capacitances (F/g) Au-MnO_2/CPCN@CC**	**Specific Capacitances (F/g) MnO_2/CPCN@CC**
0.125	503.72	339.51
0.25	485.22	300.95
0.5	393.19	276.03
1	358.76	244.51
2	352.36	209.81
4	351.71	185.14